Graphical abstract

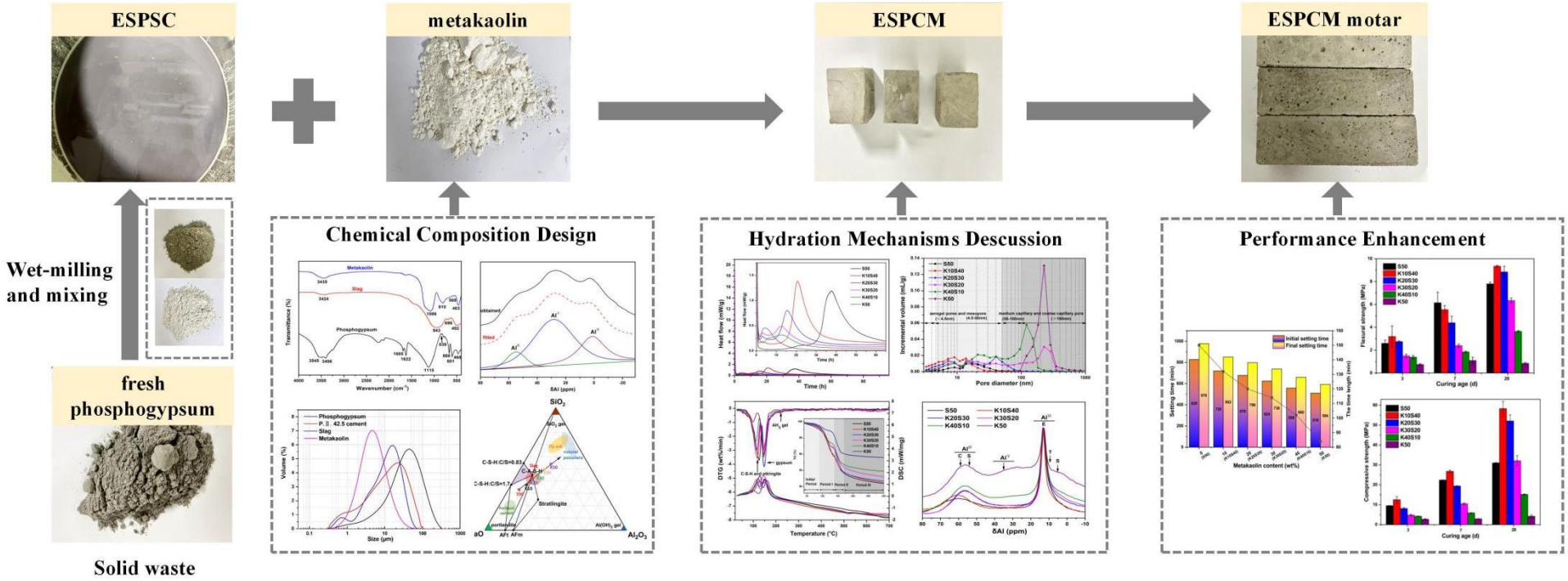

Recycling utilization of phosphogypsum in eco excess-sulphate cement: synergistic effects of metakaolin and slag additives on hydration, strength and microstructure

Ziyan Wang[a,b,1], Zhonghe Shui[c], Tao Sun[c,d,*,1], Xiaosheng Li[e], Mingzhong Zhang[f,*]

[a] *International School of Materials Science and Engineering, Wuhan University of Technology, Wuhan, 430070, China*

[b] *Guizhou Construction Science Research and Design Institute Limited Company of CSCES, Guiyang, 550000, China*

[c] *State Key Laboratory of Silicate Materials for Architectures, Wuhan University of Technology, Wuhan, 430070, China*

[d] *Wuhan University of Technology Advanced Engineering Technology Research Institute of Zhongshan City, Zhongshan, 528437, China*

[e] *School of Materials Science and Engineering, Wuhan University of Technology, Wuhan, 430070, China*

[f] *Department of Civil, Environmental and Geomatic Engineering, University College London, London, WC1E 6BT, UK*

Abstract: Landfilled phosphogypsum would cause severe environmental issues, but the waste can be recycled for preparing excess-sulphate cement, an eco-friendly alternative to conventional cement. This paper investigates the effect of metakaolin (0-50%) on early hydration, phase assemblages and mechanical properties of the excess-sulphate phosphogypsum cementitious materials (ESPCMs). Results indicate that metakaolin is related to a new exothermic peak and significantly shortens the induction period. Setting time of ESPCM pastes is reduced by 13%-38% with 0% to 50% dosage of metakaolin. More ettringite and highly disordered C-(A)-S-H gel are characterized when metakaolin dosage is below 20%, leading to 70% increase in 28-d compressive strength. With above 20% metakaolin dosage, portlandite consumption at early stage is promoted and hydration degree at late state is reduced. It turns out that 20% metakaolin dosage is efficient to optimise setting time and strength development of ESPCMs, where slag and metakaolin synergistically promote the formation of ettringite and C-(A)-S-H gel to bind the unhydrated cement particles effectively.

* Corresponding authors. E-mail addresses: sunt@whut.edu.cn (T. Sun); mingzhong.zhang@ucl.ac.uk (M. Zhang)

[1] These authors equally contributed to this work and share the first authorship.

***Keywords**:* Excess-sulphate cement; Phosphogypsum; Metakaolin; Early-age hydration, Microstructure; Strength.

1. Introduction

Phosphogypsum (PG) is a solid waste produced by the fertilizer industry, with an annual production of 10-28 million tonnes and a total amount of 400 million tonnes around the world (Huang et al., 2010; Lin et al., 2009). Using PG as a construction material has been considered an effective approach to dealing with this solid waste. Excess-sulphate phosphogypsum slag cement (ESPSC), composed of excess 40% PG, around 40-50% granulated blast furnace slag (GGBS) and a small quantity of alkali activator (Lin et al., 2010), has comparable engineering properties to Portland cement. The application of ESPSC is considered an efficient and eco-friendly way to reuse PG. However, the relatively slow hydration rate of GGBS and the impurities in PG usually lead to a prolonged setting time and reduced mechanical properties. In general, the final setting time of ESPSC paste ranges from 8 h to 20 h with different content of impurities, and the strength development is lower than that of Portland cement paste with the same water-to-binder (w/b) ratio. This problem needs urgent solution before wide applications of ESPSC.

Hydration of ESPSC essentially determines macroscopic performance. During the hydration, depolymerization of GGBS with a glassy structure occurs, and the internal links are destructed and released under the activation of alkaline and sulphate solutions. C-S-H gel gradually form a spatial network structure to connect and encapsulate unhydrated PG. Like the role of C-S-H in Portland cement, ettringite is the critical hydration product for ESPSC, a calcium sulphate activated slag cementitious system. Formation and growth of ettringite depend on the content of sulphate, aluminate and alkali activator in the systems (Duchesne et al., 1995; I. Richardson et al., 1993), which affect the setting and strength development of ESPSC paste (A Gruskovnjak et al., 2008; Matschei et al., 2005). Consequently, workability and mechanical properties can be optimised by adjusting the composition of ESPSC, mainly composed of PG, GGBS and alkali activator. The amount of PG is an essential factor affecting the ettringite formation and microstructure (Astrid Gruskovnjak et al., 2011; Hewlett et al., 2019; Singh et al., 2002). A suitable dosage of PG in the system is beneficial for mechanical properties, while its excessive addition may promote the formation of latter ettringite and precipitation of large gypsum crystals, resulting in matrix cracking. Moreover, a large amount of unreacted gypsum with a loose structure would weaken the strength of the matrix (H. Park et al.,

2016). The composition and dissolution rate of GGBS present an evident influence on the strength development of the ESPSC system (Michel et al., 2011). In the gypsum-activated slag systems, it was demonstrated that the ESPSC paste with lower aluminium-content GGBS exhibits slower strength development at early ages (Bijen et al., 1981). On the contrary, the high aluminium content leads to higher compressive strength and lower porosity after 28 d of hydration due to higher ettringite content (Bijen et al., 1981; A Gruskovnjak et al., 2008). The type and content of alkali-activator (e.g., cement, calcium oxide, sodium hydroxide, etc.) can affect the hardening rate and strength development. It is effective to enhance the early strength with the increase of alkali-activator content, whereas the continuous generation of latter ettringite after hardening in alkaline environment would result in the reduction of latter strength. It has been reported that the strength is decreased by 20% when the content of steel slag used as alkali-activator is increased from 4% to 6% (Lin et al., 2010).

To optimise the setting time and early-age strength of ESPSC, several methods have been proposed. Pre-treatment of PG by water washing, neutralization, and calcination has been found effective for modifying setting time and strength (Liu et al., 2019; M.K.Z. L.N. Zhou; Peng et al., 2000; Taher, 2007). Increasing the fineness and quality of GGBS is beneficial for the early-age strength development, where the compressive strength of pastes is enhanced from 13 MPa to 40 MPa at 28 d with the increase of the specific surface area of GGBS from 399 cm^{-1} to 650 cm^{-1}. Choosing a suitable type and content of mineral admixtures in the system is also considered a feasible method. The addition of silica fume accelerates the reaction rate and improves the latter compressive strength in the gypsum-slag system (Magallanes-Rivera et al., 2014). For instance, the compressive strength of ESPSC concrete is increased from 37.2 MPa to 46 MPa at 28 d with the addition of 5% silica fume, while the substitution of GGBS by silica fume has a limited effect on early-age strength development due to the low aluminium content in the system. So far, the early hydration behaviour and microstructure evolution of excess-sulphate phosphogypsum cementitious materials (ESPCMs) with high PG content have been rarely studied, and the effect mechanism of different supplementary cementitious materials on hydration process and hydration degree is still unclear. Thus, it is crucial and urgent to explore efficient methods for enhancing the workability and mechanical properties of ESPCMs.

Compared to silica fume and GGBS, metakaolin (MK) as an artificial material exhibits excellent pozzolanic activity (Souza et al., 2005; Tafraoui et al., 2009). The enhancement of early-age

properties of cementitious materials with the incorporation of MK can be explained by the filling effect, high pozzolanic activity, and enhanced hydration of Portland cement. Among them, the filling effect takes place at the beginning, while the effect of enhanced cement hydration mainly occurs in the first 24 h, and the pozzolanic reaction works more significantly between 7 d and 14 d. It was found that MK with high aluminium content has a profound effect on hydration kinetics and formation of ettringite in the early hydration period (Boháč et al., 2014; Fraire-Luna et al., 2006). The nucleation of MK can accelerate the hydration rate of Portland cement (Shi et al., 1995). The rapid formation of controllable ettringite in initial period could promote the hydraulic performance of the matrix and facilitate strength development obviously (Shi et al., 1995). The incorporation of MK with high aluminium content can promote cement hydration and early formation of ettringite, which is considered a promising method to improve the workability and mechanical properties of ESPCM, while the underlying mechanisms have not been extensively addressed.

The main purpose of this work is to investigate the early hydration behaviour and microstructure evolution of ESPCMs containing different MK dosages (i.e., 0%, 10%, 20%, 30%, 40% and 50%). A series of advanced techniques including Isothermal conduction calorimetry (ICC), X-ray diffraction (XRD), Fourier transform infrared spectroscopy (FTIR), derivative thermal gravimetric-differential scanning calorimetry (DTG-DSC), ^{27}Al solid nuclear magnetic resonance (^{27}Al NMR) and mercury intrusion porosimetry (MIP) are used to characterise the effects of GGBS and MK on heat evolution, hydration products and pore structure of ESPCMs. Based on the measured hydration degree and hydration kinetics, the effect of MK dosage on setting time and mechanical properties of ESPCMs is explored. Afterwards, the enhancing mechanism of hydration and strength development is discussed further to optimise the mix proportions and provide a design guide of ESPCMs with desired engineering properties for practical applications.

2. Experimental program

2.1 Raw materials

PG, cement, GGBS and MK were used for this study, the chemical composition and particle size distribution of which were presented in Table 1 and Fig. 1, respectively. PG (D_{50}=33.9 μm) regarded as sulphate was mainly composed of 81.16% gypsum, quartz and impurities including phosphorus, fluorine impurities, etc. Cement (D_{50}=11.6 μm) served as alkali activator, the main mineral composition of which was calculated using the Bogue method and listed in Table 2.

Table 1. Chemical composition of raw materials (wt%) by XRF.

Oxide	Al_2O_3	SiO_2	Fe_2O_3	CaO	K_2O	TiO_2	SO_3	P_2O_5	Na_2O	MgO	F	LOI
Phosphogypsum	1.09	7.5	0.44	27.05	0.6	0.12	37.75	0.948	0.17	0.06	1.83	20.77
P Ⅱ 42.5 cement	6.45	21.75	3.24	58.02	0.74	0.51	2.47	0.25	0.14	2.25	-	3.8
Slag	15.16	32.95	0.21	40.14	0.4	0.71	2.27	0.01	0.27	7.29	-	0.58
Metakaolin	38.72	56.71	0.77	0.06	0.56	0.28	0.13	0.45	0.38	0.11	-	1.79

Table 2. Main mineral phases in cement.

Phase	C_3S	C_2S	C_3A	C_4AF	$C\bar{S}$
Volume fraction (%)	45.60	27.95	11.61	9.84	4.19

GGBS and MK were combined in a pozzolanic mixture, where the CaO/SiO_2 ratio of GGBS and Al_2O_3/SiO_2 of MK were 1.22 and 0.68, respectively. The main difference between MK and GGBS was the higher content of calcium oxide in GGBS and higher content of aluminium oxide in MK. The GGBS can be regarded as a (Si+Ca) system, and MK a (Si+Al) system (Lothenbach et al., 2011). Different components of active phases would affect the content and type of hydration products, especially the ettringite and C-(A)-S-H gel with various Ca/Si and Al/Si ratios and structures in ESPCMs. Compared with GGBS (D_{50} =10.9 μm), MK (D_{50}=4.4 μm) with monolithic or laminar morphosis has a higher specific surface area and water absorption, leading to the increase of hydration rate and flow loss in fresh paste (Sun, 2019). Hence, a sort of polycarboxylic superplasticizer supplied by Sobute New Materials Company Limited was added to ensure all mixtures have the same workability during the preparation process of mortar.

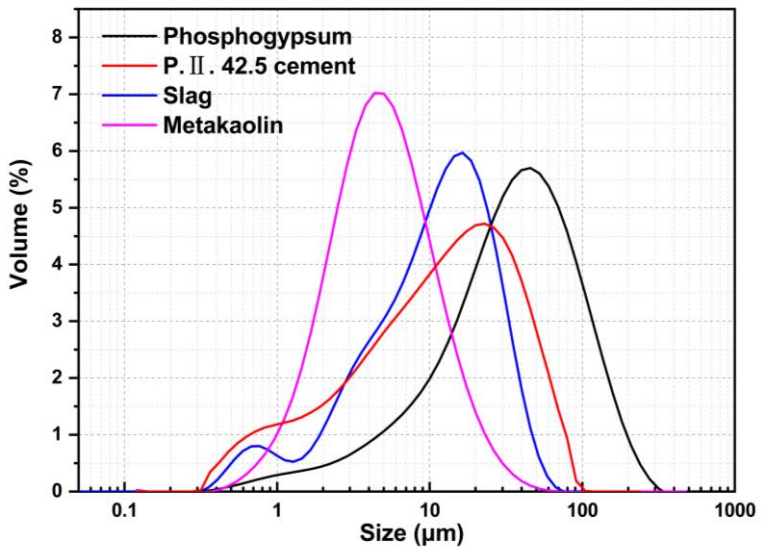

Fig. 1. Particle size distribution of raw materials.

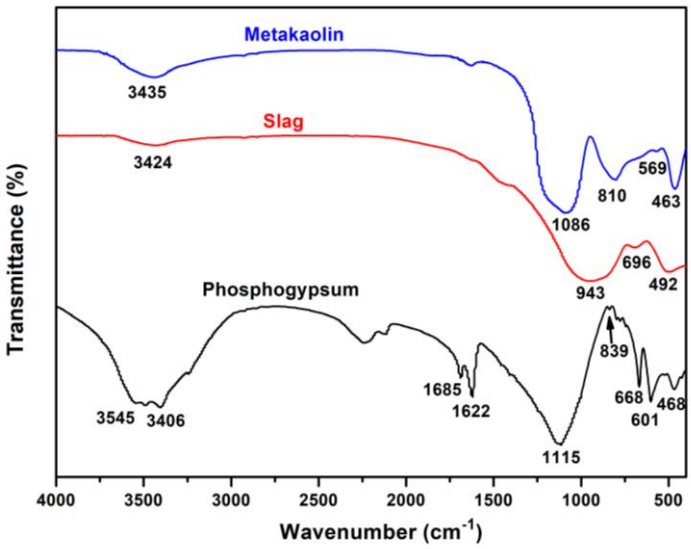

Fig. 2. FTIR spectrum of raw materials.

Fig. 3 illustrated the ^{27}Al NMR spectra of GGBS and MK. The broad resonance covering a range from 80 ppm to -30 ppm was composed of 3 overlapped gaussians corresponding to aluminium oxide in different chemical environments. The GGBS used in this study found three fitted resonances at about 1.9 ppm, 33 ppm and 58.9 ppm, suggesting the existence of tetrahedrally, pentahedrally and hexahedrally coordinated aluminium sites, repectively. For MK, the resonances at 1.9 ppm, 28 ppm and 55 ppm in the spectrum represented aluminate sites in tetrahedral, pentahedral, and octahedral coordination, respectively. The tetrahedrally and pentahedrally coordinated aluminium were the primary coordination forms in GGBS, while more aluminium with hexahedrally coordination existed in MK. In general, the aluminium in tetrahedrally and pentahedrally coordinated aluminium possessed higher reactivity.

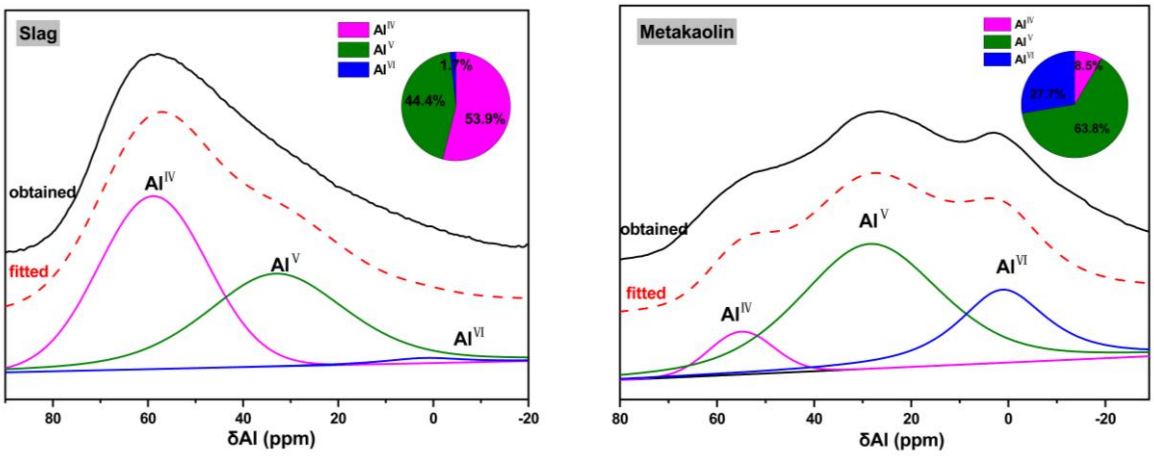

(a) (b)

Fig. 3. ^{27}Al NMR spectra of (a) GGBS and (b) MK. (Adding the relative mass of tetrahedrally, pentahedrally and hexahedrally coordinated aluminium sites)

2.2 Mix proportions

Table 3 showed the mix proportions of ESPCMs in this study, which were determined according to the previous studies. The chosen contents of modified PG and cement were 45% and 5%, respectively, of the powder precursors by mass in all mixtures to ensure sufficient latter strength development and apply as higher PG dosage as possible (Lin et al., 2010). The w/b ratio for all mixtures was kept consistent as 0.5, while the rest (50%) was the combination of GGBS and MK, where the content of GGBS and MK were varied in the range of 0%-50%, respectively. Based on the reference only contained slag (i.e., S50), using MK substituted GGBS gradually to study the effect mechanism on microstructure and properties of ESPCM, where the optimal proportion for actual application was obtained. In Table 3, the labels 'S' and 'K' stood for GGBS and MK, respectively, and the numbers (i.e., 10, 20, 30, 40, 50) denoted the contents of the corresponding mineral admixtures. For instance, the sample label 'S50' contained 50% GGBS but no MK, which was regarded as a reference. Additionally, 'K10S40' represented the mixture with MK and GGBS dosages of 10% and 40%, respectively.

Table 3. Mix proportions of specimens (wt%)

Sample label	Modified phosphogypsum (wt%)	P II 42.5 cement (wt%)	Slag (wt%)	Metakaolin (wt%)	Water/binder (w/b)
S50	45	5	50	0	0.5
K10S40	45	5	40	10	0.5
K20S30	45	5	30	20	0.5
K30S20	45	5	20	30	0.5
K40S10	45	5	10	40	0.5
K50	45	5	0	50	0.5

Fig. 4 demonstrated the hydrate phases and sample components in the CaO-SiO_2-Al_2O_3 system, referring to the chemical composition analysis shown in Table 1. The composition was farther away from the vertex of calcium oxide in the phase diagram with the increase of MK dosage. Due to the lower calcium content and higher aluminium content compared to GGBS, MK was expected to react in the excess-sulphate environment to form additional ettringite and facilitate the transformation of aluminium into C-S-H gel in comparison with S50 at a low MK substitution level. The decrease of Ca/Si ratio would occur in the structural transformation of C-S-H gel, e.g., the disordered jennite-like

unit ($9CaO{\cdot}6SiO_2{\cdot}11H_2O$) to the tobermorite-like structure containing defects in the silicate dreierketten chains ($0.83CaO{\cdot}SiO_2{\cdot}1.5H_2O$) (I. Richardson et al., 1993; Taylor, 1993; J. Wei et al., 2019). When the replacement level was high, the shortage of portlandite derived from the hydration of GGBS and cement even may prevent the continuous hydration process of MK. Therefore, K50 containing 50% MK was designed as the extreme case and used to explore the effects of GGBS and MK on the hydration process, respectively.

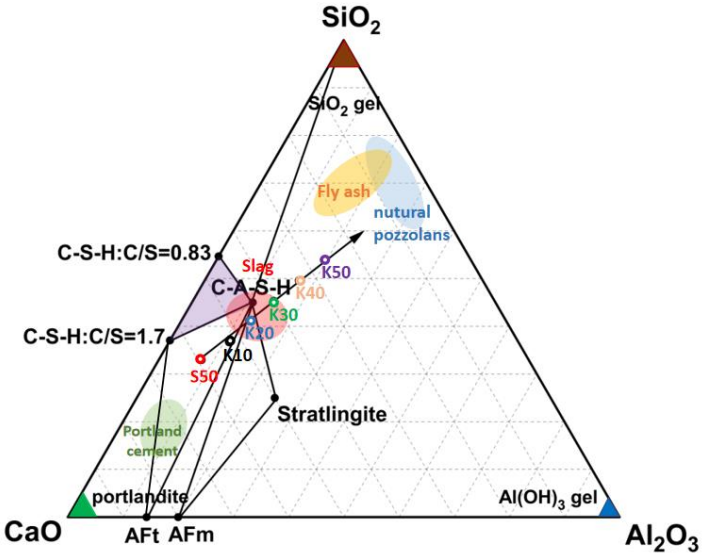

Fig. 4. Hydrate phases and sample components in the CaO-Al_2O_3-SiO_2 system.(Revised this picture as Reviewer#1 suggested)

2.3 Sample preparation

Fig. 5 illustrated the whole manufacturing process of ESPCMs, including the pre-treatment of PG and preparation of ESPCMs, where the pre-treatment of PG was a necessary step to mitigate the impact of impurities on workability and mechanical properties. The pH value will exceed 12 when containing 3%-4% cement, of which the improvement rate displayed a reduction with further incorporation. Therefore, the moisture content of fresh PG was determined firstly, and then the wet-milling of mixtures (namely pre-treatment of PG) lasted 30 min, which contained fresh PG, GGBS, and cement at 47:1:2 with a water-to-solid ratio of 0.6. The modified PG was obtained after curing the mixture for 24 h to precipitate impurities adequately and mixed with other raw materials for 4 min as per the designed mix proportions given in Table 3 to prepare different ESPCM samples. The total water consumption containing the moisture in fresh PG and water demanded in pre-treatment and preparation processes was kept the same for all mixtures with a constant w/b ratio of 0.5. The

fresh ESPCM pastes were moulded as 40 mm × 40 mm × 40 mm cubic samples and cured for 48 h at room temperature before demoulding. Similarly, the rectangular mortar specimens in size of 40 mm × 40 mm × 160 mm with a constant w/b ratio of 0.5 and binder-to-sand of 1/3 were prepared by mortar mixer and compacted on a vibrating table, which was carried out for mechanical properties tests (Standard, 1999). All demoulded specimens were stored in a standard curing room with a temperature of 20 ± 2 °C and relative humidity of 96 ± 2% until the ages for testing.

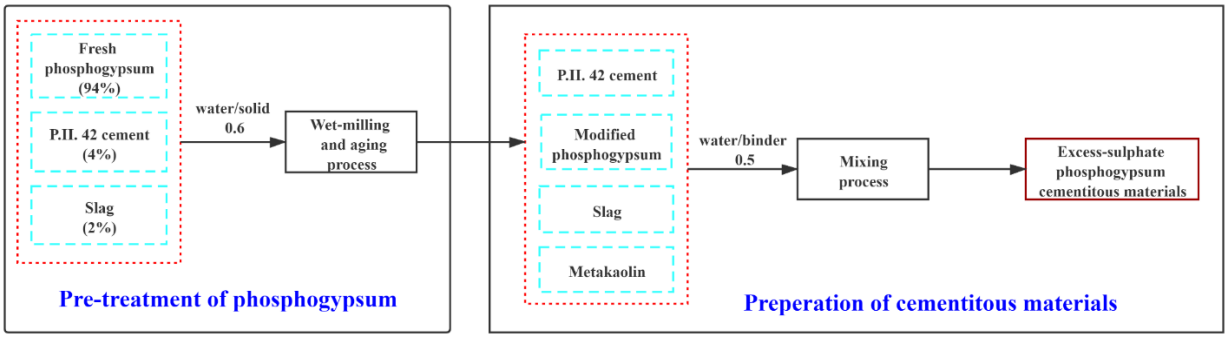

Fig. 5. ESPCMs preparation process in this study.

2.4 Test methods

2.4.1 Isothermal conduction calorimetry (ICC)

To estimate the effect of MK on the early hydration of ESPCMs, the heat evolution of fresh pastes was measured using a TAM-Air isothermal calorimeter. All pastes were injected into the glass ampoules of calorimetry, and another glass ampoule containing the same weight of de-air water was regarded as a reference. All samples were tested immediately after contact with water at 20 °C over 96 h, and the heating rate was controlled at 0.1-2.0 °C/min with an accuracy of 0.1 °C.

2.4.2 Setting time test

The setting time was measured to verify whether the addition of MK could effectively accelerate the hydration rate by measuring the penetration depth of a Vicat needle in combination with the heat flow results. The water required for the normal consistency was firstly determined as per GB/T 1346-2001 (Strandard, 2011), and then the measurement started once pastes contacted with water. The measurement was taken every 20 min before the initial setting time and then shortened to every 3 min when approaching the initial and final setting time.

2.4.3 X-ray diffraction (XRD)

Solvent change was taken at 28 d to stop further hydration of sample before the hydration products

and microstructure were characterised using XRD, FTIR, TG-DSC, and ^{27}Al NMR. The inner fragments of cubic paste with a diameter of less than 5 mm were submerged in ethanol (solid-to-liquid volume ratio of 1:240) for more than 1 month, where the ethanol was renewed every two days. The obtained fragments were vacuum dried at 40 °C for one week and crushed into powder passing through a 63-μm sieve for tests. XRD was carried out to characterise the mineral compositions of specimens using Bruker D8 Advance diffractometer with Cu Kα X-ray source in the condition of 40 kV and 40 mA. All ESPCM samples were scanned in the range between 5° and 30° with per step size of 0.02° (2θ). The relative mass (W) among different minerals can be determined through XRD/reference intensity ratio (RIR) analysis when the compositions of hydration products were relatively simple (I. Richardson et al., 1993; Taylor, 1993).

2.4.4 Fourier transform infrared spectroscopy (FTIR)

The FTIR spectra can be used to identify the bonding characteristics of substance with crystalline and amorphous phases as a complement of XRD, where the intensity and width of bands are also considered indicators to evaluate the content of substance and polymerization degree of gel. Prior to the test, the mixture of sample powder and potassium bromide with a ratio of 1:100 was compacted as flakes. An FTIR instrument (Nexus spectrometer) with scanning in the mid-infrared region of 4000 cm^{-1} to 400 cm^{-1} was employed to characterise the hydration products at room temperature.

2.4.5 ^{27}Al Nuclear magnetic resonance (^{27}Al NMR)

The hydration products, including the active aluminium phase in ESPCMs, were investigated using the ^{27}Al NMR spectrum, which was employed to make a rough evaluation of hydration degree. Combined with the oxides content in each sample, the deconvolution of obtained ^{27}Al NMR patterns was regarded as a feasible method for quantitative analysis, providing further information to estimate the effect of MK on the hydration process. The ^{27}Al NMR spectra were recorded using a Bruker Avance-400 NMR spectrometer with a magnetic intensity of 9.4 T. About 100 mg sample was compacted in the 4 mm rotor and spun at a speed of 10 kHz. The pulse width of 1 μs and recycle delay of 2 s with 1024 scans were applied for ^{27}Al NMR, the chemical shifts (in ppm) of which were relative to the aqueous solution of $Al(NO_3)_3$.

2.4.6 Derivative thermogravimetry-differential scanning calorimetry (DTG-DSC)

DTG-DSC was carried out on specimens to estimate the mass of non-evaporable water in PG and hydration products so as to further verify the quantitative analysis of ^{27}Al NMR and facilitate the

comparison of the contents for the same substances in each sample. The samples were thermally treated from 25 °C to 1000 °C at 10 °C/min under the air atmosphere using a TA SDT Q 600 calorimeter.

2.4.7 Mercury intrusion porosimetry (MIP)

Pore structure was highly related to the hydration process, which strongly affected the mechanical properties development and durability of ESPCMs. MIP was performed to characterise the pore structure of ESPCM specimens using an AutoPore IV-9500. Before testing, inner fragments were dried using acetone as a solvent exchange method and kept in a vacuum drying oven for 4 h at 105 °C. The density, surface tension, and contact angle of mercury on cement paste were assumed to be 13.534 g/mL, 485 dyn/cm, and 130°, respectively, and thus the measured range of pore size in diameter was between 3 nm and 360 μm.

2.4.8 Compressive and flexural strength test

In accordance with GB/T 17671-1999 (Standard, 1999), the compressive and flexural strengths of all mortar specimens at 3, 7, and 28 d were measured using a universal tester with a loading rate of 2.4 kN/s and 0.6 kN/s, respectively. Three water-saturated mortars with dry surfaces were measured for each mixture, and the average value and standard deviation were obtained and used for further analysis.

3. Results and discussion

3.1 Hydration heat evolution

Fig. 6 shows the heat flow of all pastes within 96 h. The heat flow curve of the reference sample with 50% GGBS are featured with two distinct peaks, similar to that of the super sulphate cement (SSC), consistent with previous studies. In general, the hydration heat flow curve of SSC, in which cement acts as the activator, can be divided into three stages: (1) dissolution and formation of initial ettringite, (2) induction period, and (3) rapid hydration of GGBS (Gijbels, Nguyen, et al., 2019; Liu et al., 2019). However, the calorimetric curves describing the heat flow against the time of mixtures containing MK indicate a new peak at the induction. With the further increase of MK, the time required to achieve the maximum rate of heat evolution becomes shorter, and the cumulative heat is decreased.

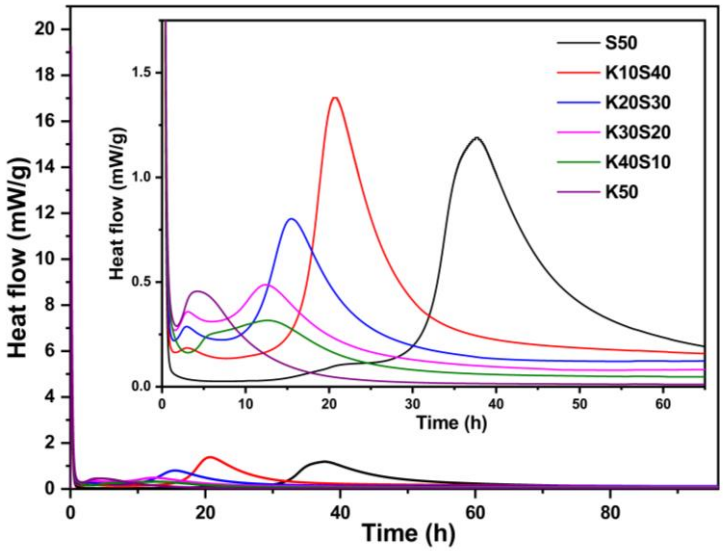

Fig. 6. Hydration heat flow of ESPCM pastes.

Table 4 lists the cumulative heat release and time position of all peaks derived from the heat evolution curves. An immediate increase in the evolved heat takes place within approximately 3 min after the contact of samples with water and lasts for 30 min. Concurrent with the dissolution of PG, the impurities such as soluble P_2O_5, fluoride, and residue acid are released from the surface or crystal lattice of PG continuously, which exists stably as H_3PO_4, $H_2PO_4^-$, HPO_4^{2-}, PO_4^{3-}, and F^- during the initial period. As the hydration of cement clinkers proceeds, the rate of heat release accelerates due to the formation of ettringite with the rapid rise of pore solution pH to 12.6 in a short period because of the continuous generation of alkali hydroxides and calcium hydroxide as described by Eqs. (1) and (2) (Jin et al., 2003). Several reactions occur in sequence or synchronously, which are affected by various factors in this period. Hence, there is no discernible difference between the binders and irregularity in terms of rate (do Carmo Holanda et al., 2017; Gijbels, Iacobescu, et al., 2019; Radwan et al., 2003, 2005).

$$3CaO{\cdot}Al_2O_3 + 3CaSO_4{\cdot}2H_2O + 26H_2O \rightarrow C_3A{\cdot}3CaSO_4{\cdot}32H_2O \text{ (ettringite)} \quad (1)$$

$$3CaO{\cdot}SiO_2 + 3.9H_2O \rightarrow C_{1.7}SH_{2.6} + 1.3Ca(OH)_2 \quad (2)$$

Table 4. Characteristics of main hydration heat release peaks within 96 h.

Sample label	Cumulative heat release (J/g)			Time of heat flow-max (min)		
	Period Ⅰ	Period Ⅱ	Period Ⅲ	Peak Ⅰ	Peak Ⅱ	Peak Ⅲ
S50	9.54	-	88.48	5	2249	-
K10S40	9.58	7.32	85.49	4	174	1228
K20S30	11.64	9.10	62.01	4	176	929

K30S20	11.22	9.81	43.21	4	185	743
K40S10	8.80	16.64	18.05	3	347	731
K50	12.84	21.02	-	3	252	-

Note: "-" not detected

As seen in Fig. 6, S50 features the longest induction (30 h) compared to mixtures with various MK contents (K10S40 to K50). As the MK dosage increases from 10% to 50%, the intensity of peak II presents a significant enhancement, where the cumulative heat release is increased from 7.32 J/g to 21.02 J/g in period II. Addition of MK shortens the duration of induction, where a continuous heat release is observed, suggesting that MK could promote the hydration of ESPCMs at early ages. Given that the heat release is proportional to the degree of hydration, the relationship between MK dosage and cumulative heat release in period II and III is investigated and presented in Fig. 7. A good correlation between the addition of MK and heat release can be observed in period II, where the incorporated MK with small particle size provides additional surface area for heterogeneous nucleation of hydration products, and promotes the hydration, especially for cement. This effect from MK is unique, considering the distinct physical and chemical properties between MK and GGBS.

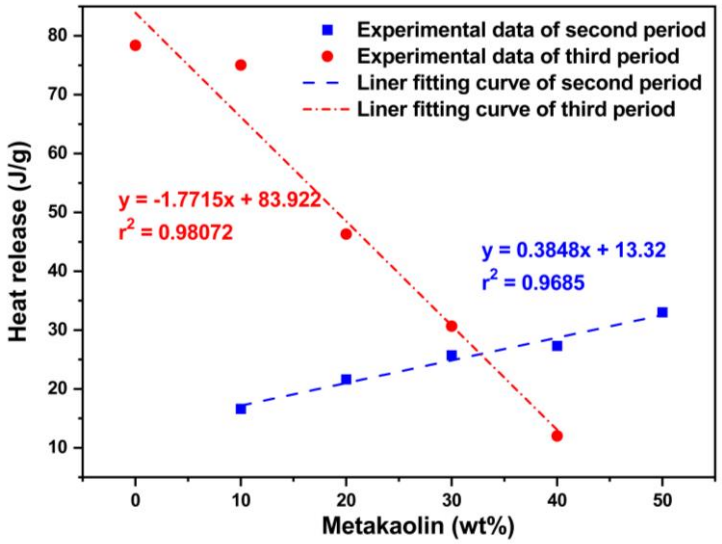

Fig. 7. Relationship between the cumulative heat release to second period, third period and the content of metakaolin.

The acceleration period (period III) can be ascribed to the assemblage of C-S-H gel, which is regarded as a dominant factor for the strength development of CaO-activated GGBS systems (Min et al., 2013), accompanied by a significant heat release. As the MK dosage increases from 10% to 40%, the peak heat flow in period III decreases from 1.38 mW/g to 0.31 mW/g, referring to S50 (around

1.19 mW/g). There exists a good correlation between cumulative heat release and MK dosage in period III, where no peak can be observed for specimen K50. The solubility of amorphous silica is sensitively affected with the increase of pH between 12 and 14, so that the availability of sufficient hydroxyl ions to maintain the pH determines whether the hydration reaction of supplement cementitious materials can proceed. As demonstrated in (Boháč et al., 2014), more portlandite is consumed in cement-MK binder compared to cement-GGBS system with the same dosage, and thus a more significant drop of the pH and hydration rate can be observed for a higher replacement level of GGBS by MK.

Compared to that of Portland cement (P. II. 42.5) paste (nearly 334 J/g), the cumulative heat release of ESPCM pastes is about 70% lower, where the specimen containing 50% GGBS only reaches 98.48 J/g, as shown in Fig. 8. With increasing MK content from 10% to 50%, the cumulative heat curves for the phases substituted by MK tend toward convergence and decline from 102.28 J/g to 33.86 J/g. It is indicated that MK affects the hydration kinetics as well as the cumulative hydration, which is associated with the degree of hydration for pastes. The experimental results of enhancement of heat release rate and cumulative heat release suggest that the main hydration takes place in period III.

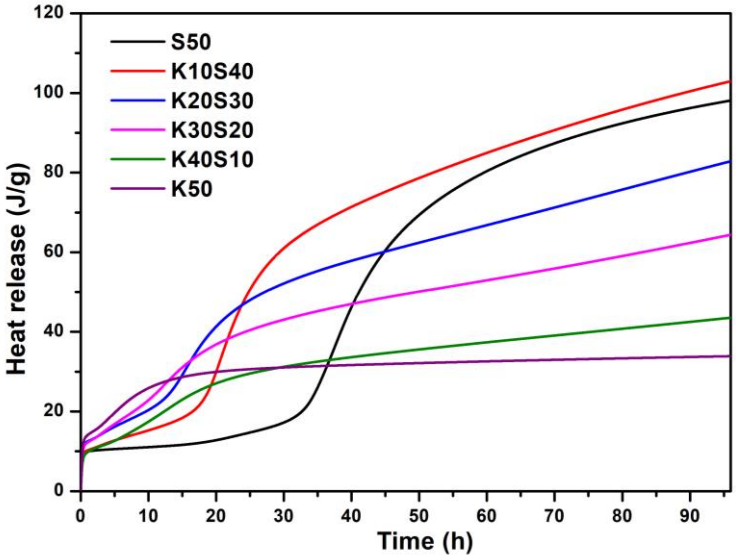

Fig. 8. Cumulative hydration heat of ESPCM pastes.

3.2 Setting time

Fig. 9 displays the initial and final setting time of ESPCM pastes. Overall, the reference sample with 50% GGBS possesses a longer setting time in comparison with those containing MK. With the

replacement of GGBS by MK, the initial and final setting time is reduced from 828 min to 510 min and 978 min to 594 min, respectively. The initial substitution of 10% MK presents a prominent effect on the reduced setting time, which implies that the existence of MK can speed up the hydration rate of Portland cement and SCMs, leading to a shorter induction period. With the further addition of MK, the accelerated effect is weakened, and the difference between initial and final setting time also presents a decline, where the distinction decreases from 150 min (in S50) to 84 min (in K50).

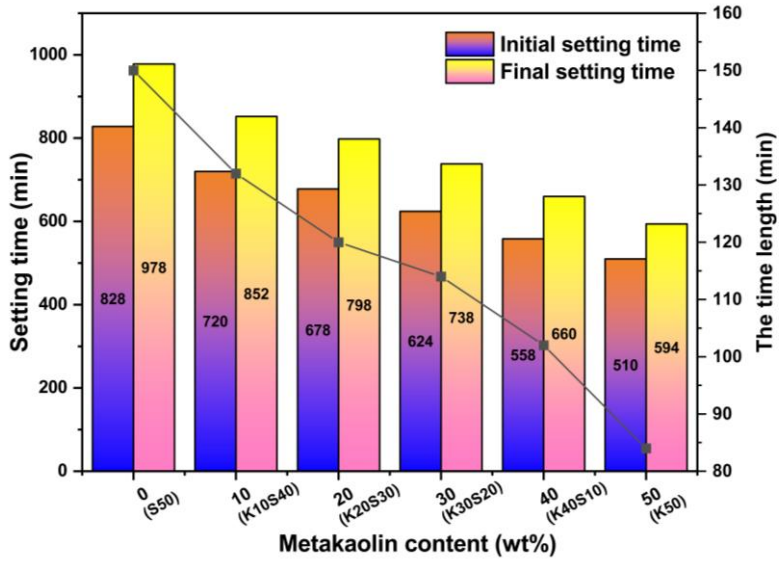

Fig. 9. Initial and final setting time of ESPCM pastes. (This picture is optimised without change any data)

In ESPCM pastes, the retarding action can be attributed to the effect of impurity precipitation on cement hydration. The retarding effect due to the steady dissolution of Ca^{2+} and formation of supersaturated portlandite is affected by calcium phosphate and calcium fluoride (Speight, 2017). When the environmental pH value exceeds 10.8 (X. Li et al., 2017), the successive increase in soluble phosphorus presented as PO_4^{3-} as well as its relation to fluoride ions would be precipitated on the particle surface of cement clinkers and the hydrate nuclei, preventing the continuous growth of pH value and nucleation of C-S-H gel (Bishop et al., 2003; do Carmo Holanda et al., 2017; Jiahui et al.; Tabikh et al., 1971). Therefore, the rate of dissolution and hydration of GGBS decreases remarkably at the low pH value resulting from the retarded residual PO_4^{3-}. An extended induction is required to increase the alkali hydroxides concentration, where the destruction of GGBS can be facilitated (Sujin Song et al., 1999; S Song et al., 2000). MK obtained from the destruction of hydroxyl groups which exists in kaolinite layer structure at high temperatures (Caladrone et al., 1994) shows a larger internal

pore size and specific surface area (Yuheng et al., 2006). For fluoride ion, it can be absorbed by ligand exchange at the aluminol groups (Al/OH), the adsorption capacity of which is influenced by pH and fluoride ion concentration (Ioannou et al., 1997; Landry et al., 2009; S. Wei et al., 2014). The dihydrogen phosphate can be absorbed on the surface of the aluminium to form a monolayer of adsorbate molecules or furthermore (Jha et al., 2008; Nabbou et al., 2019). Thus, more phosphate and fluoride ions are removed from the solution theoretically with the increasing dosage of MK to diminish the retarding action, leading to a shorter induction period (Fig. 6) and reduced setting time (Fig. 9). Moreover, the alkali-active process of MK induced by the destruction-coagulation-condensation-crystallization mechanism occurs promptly at different pH values (Chao et al., 2010; Glukhovsky et al., 1980; Wang et al., 2003). An additional silicon or excellent condition is provided for the generation of C-S-H nuclei (Michel et al., 2011) to accelerate the hydration rate of Portland cement and promote the hardening of pastes. Even so, the rapid formation of needle-like ettringite on the surface of cement as the pH value reaches 12.46, resulting in a reduction in cement hydration rate (M. Collepardi et al., 1978; MARIO COLLEPARDI et al., 1979). The retarding effect would occur continuously until the film of ettringite ruptures under crystallization pressure (Hargis et al., 2013; Qian et al., 2017).

3.3 Hydration products

3.3.1 Chemical composition

Fig. 10 demonstrates the XRD results of binders at 28 d. In addition to the existence of ettringite and unhydrated PG with the characteristic peaks located at 9.1° and 11.6° 2θ respectively, other hydration products such as portlandite (main peak at 28.7° 2θ) and AFm (main peak at 9.5° 2θ) can't be observed for the specimens with or without MK, implying that the generated portlandite is rapidly consumed for pozzolanic activity and the ettringite maintains stable in the sulphate-rich environment. Because of the high crystal phase content, no significant diffuse peak corresponding to hydration products with an amorphous state can be observed in XRD patterns. In general, XRD observation shows no changes in diffraction distribution of hydration products in pastes, suggesting that the incorporation of MK does not cause the transformation of hydration products, which is related to their chemical composites. It is worth noting that the change of MK content leads to the different intensity of ettringite and gypsum peaks in ESPCM pastes, indicating a variation in hydration degree of pastes containing different MK contents. Although the accurate quantitative analysis of hydration products

in samples cannot be achieved with the absence of the internal standard, the hydration degree of specimens after 28 d can be compared roughly based on the relative peak intensity of ettringite and gypsum. Compared to S50, the ettringite peak intensity of specimens K10S40 and K20S30 is higher, and the relative peak intensity (ettringite/gypsum) gradually decreases with the further incorporation of MK. A reduction in hydration degree brings an enhancement on the peak intensity of the gypsum, while the remaining gypsum in K50 is the highest, which serves as filler with porous structure, weakening the strength of the matrix.

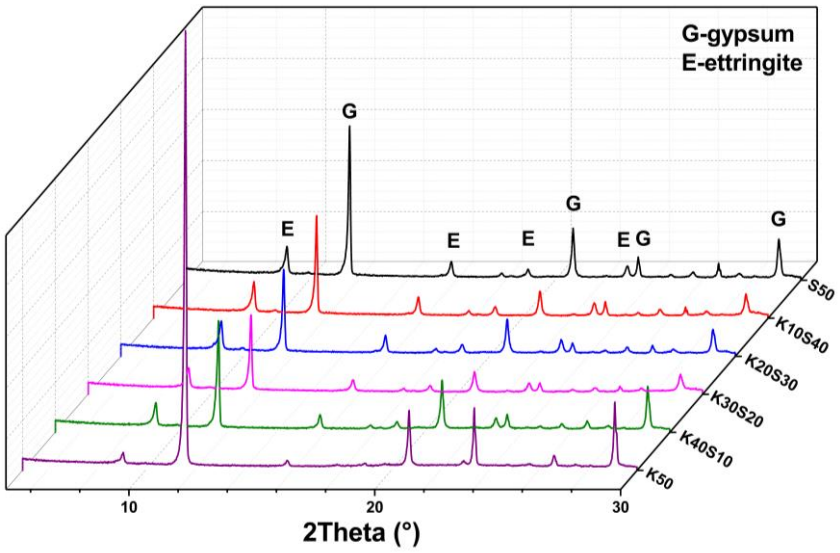

Fig. 10. XRD patterns of ESPCM binders at 28 d.

Fig. 11 illustrates the infrared spectra of all binders containing MK at 28d, where all curves are normalized, referring to the characteristic band at 1116 cm^{-1} due to the same content of SO_4^{2-} in each sample. The distribution of characteristic bands is mainly located in four regions and displays slight changes between different specimens, suggesting the addition of MK does not affect the types of hydration product, which is consistent with the XRD analysis above. The high-frequency region located between 4000-2500 cm^{-1} can be used to analyse the O-H stretching vibrations, where different characteristic bands correspond to the bond water in a different structural environment, such as $Al(OH)_6$ or water molecules. The asymmetric and symmetric O-H stretching vibrations of $Al(OH)_6$ octahedra can be distinguished by the typical band at 3637 cm^{-1} (Scholtzová et al., 2015). As the primary hydration product, the structural units of ettringite are composed of the columns of $\{Ca_6[Al(OH)_6]_2\times 24H_2O\}^{6-}$ (A Gruskovnjak et al., 2008) with intercolumn channels substituted by SO_4^{2-} anions and additional H_2O molecules (Myneni et al., 1998). With the increase of MK dosage

from 0% to 50%, the intensity of this band tends to enhance first and then decline, indicating the different hydration degrees of samples. In addition, other bands in the region of 4000-1600 cm^{-1} are related to the O-H vibrations existing in water molecules (L.Frost et al., 2013).

The asymmetric stretching vibrations of the SO_4^{2-} distinguished by the broad intense band at 1116 cm^{-1} look stronger and wider with the further incorporation of MK. Although it is difficult to confirm whether the main inducements are ettringite or untreated gypsum (L.Frost et al., 2013; Moore et al., 1970), the generation of ettringite tends to narrow and sharpen the band in comparison with gypsum. Additionally, the bands at 669 cm^{-1} and 602 cm^{-1} are noticed in all ESPCM samples, MK and PG, recognised as the complex bands consisting of δ(Al-O-H), δ(S-O), and δ(Ca-O-H) (Scholtzová et al., 2015). The Si-O stretching vibration in the Q^2 tetrahedra of C-(A)-S-H gel is recognized by the band at 973 cm^{-1}(Andrade et al., 2019; Bosque et al., 2014), and the transformation of the which from higher wavenumbers to lower wavenumber with the enhancement in Ca/Si and the decline of polymerization of C-(A)-S-H gel (Kapeluszna et al., 2017). The generated C-A-S-H gel produced by the hydration of Portland cement presents a higher Ca/Si within 1.2-2.3 generally, of which the solubility increases rapidly when the Ca/Si is larger than 1. While, the range of Ca/(Si+Al) value for hydration product extends to 0.7-2.4 by adding supplementary cementitious materials with rich aluminium phase, implying the generation of aluminosilicate polymer (Barnes et al., 2002). As the transformation of aluminium derived from MK into the C-S-H gel chain decreases the crystallinity, the specimens containing 10%-30% MK display a larger amplitude of band as compared with S50. This implies that the substitute of GGBS by MK within limits can improve the polymerization of C-A-S-H gel with lower Ca/Si and higher Al/Ca ratios (Fernández-Jiménez et al., 2005; Puligilla et al., 2015), while the excess substitution may lead to a low hydration degree due to the absence of portlandite, which is consistent with the ICC and XRD results of K50. Additionally, the remarkable bands at 810 cm^{-1} and 460 cm^{-1} assigned as the stretching and bending vibration of Si-O respectively are noticed in the sample incorporated 50% MK, meaning the existence of unreacted MK in the matrix.

The second derivative of the measured transmittance (T) over the wavelength (W): d^2T/dW^2 is obtained, as Fig. 11b shown, aiming to verify the different signals and differentiate the wavenumbers further. Published data has demonstrated that the characteristic band of S-O centred 1004 cm^{-1} can deconvolute to the peaks at 1116 cm^{-1}, 1143 cm^{-1}, 1171 cm^{-1}, and 1098 cm^{-1} corresponding to the degenerate and non-degenerate modes of SO_4^{2-} units occupying different positions (Scholtzová et al.,

2015). Therefore, the signals located within 1000-1200 cm^{-1} are identified as S-O bands in all samples. In addition, the signals associated with the composite bending vibrations of Ca-O-H and Al-O-H at 776 cm^{-1} and 797 cm^{-1} tend to be narrow and sharp with the further incorporation of MK, implying the existence of unreacted MK in the matrix. Similarly, the characteristic bands at 1050-1100 cm^{-1}, 1003 cm^{-1}, and 875 cm^{-1} present higher intensity in K50 due to the low hydration degree. As an index to recognise the existence of C-A-S-H gel, the main band for asymmetric stretching of the AlO_4^- group in Al-O-Si bonds (i.e., at 873 cm^{-1}) exhibits a similar trend with the band at 973 cm^{-1}, where the intensity is more distinct in K20S30 (Bernal et al., 2011; Fang et al., 2020). It means that more aluminium provided by MK promotes the generation of C-A-S-H gel with a higher degree of polymerization and cross-linking, contributing to higher permeability and lower durability (Fang et al., 2020). The depletion of the characteristic band in specimen K50 shows the limited generation of C-A-S-H gel when GGBS is fully replaced with MK. In addition, the Al-O-H symmetric stretching vibration is noticed in the range of 1034-1079 cm^{-1}. The $Al(OH)_m^{3-m}$ released by GGBS and MK with high content tend to exist in the form of AH_3 gel with the absence of portlandite, and thus it is regarded as a complement of XRD analysis to identify the existence of AH_3 gel as it has low crystallinity or tends to be amorphous. (The explains are optimised further)

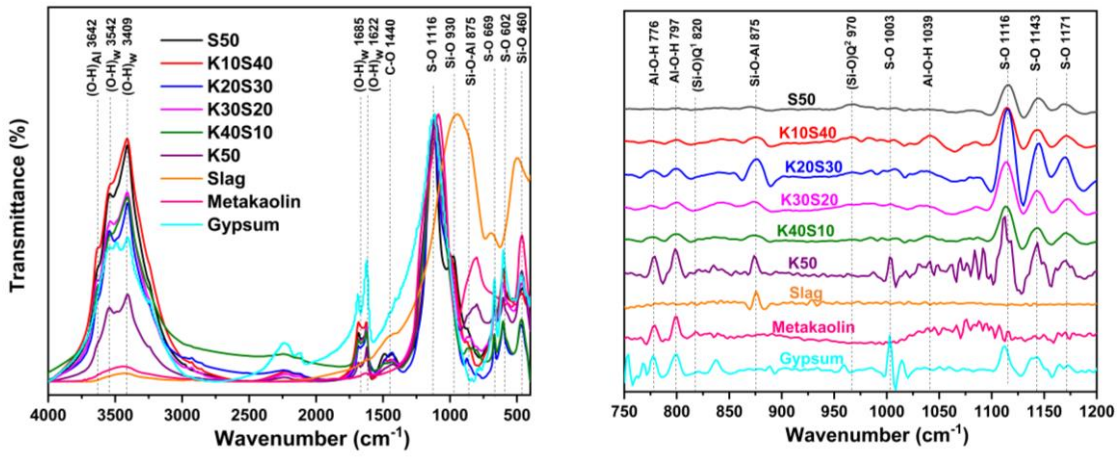

(a) (b)

Fig. 11. FTIR spectra of ESPCM binders at 28 d (a) transmittance (T) vs. wavelength (W); (b) 2nd derivative of the transmittance d^2T/dW^2 vs. wavelength. (This picture is optimised without change any data)

3.3.2 Phase content

In combination with the qualitative analysis of hydration products, the mass of different hydration

products is determined further using ^{27}Al NMR and DTG-DSC. The obtained ^{27}Al NMR spectra of all pastes are illustrated in Fig. 12. The signals for aluminium phases show two sharp peaks located at around 13 ppm and 60 ppm, where the relative intensity ($R= I_{13\ ppm}/I_{60\ ppm}$) tends to grow and then declines with the increase of MK content, implying the generation of ettringite (Andersen et al., 2003; I. G. Richardson, 2000; Scrivener et al., 2016; Skibsted et al., 1993) and C-A-S-H gel (Deng et al., 2020; Pardal et al., 2012). The signal located in 40-70 ppm transforms from the high chemical shift to the low chemical shift, implying the uptake of aluminium in C-A-S-H gel with the various cross-link degrees. It has reported that the aluminium with tetrahedral coordination situated at 73 ppm and 68 ppm are assigned as bridging Al in the Q^1(I) and Q^1(II) sites, respectively, to realize the charge-balanced with monovalent and divalent cations in the silicate network. The presence of resonances at 62 ppm and 58 ppm are associated with highly cross-linked aluminium in C-A-S-H gel, where the function of the aluminium phase at 58 ppm is certainly not charge-balanced with divalent cations (Myers et al., 2015; S. M. Park et al., 2016; Seo et al., 2021). In addition, the existence of AH_3 gel, unhydrated GGBS and MK in ESPCM pastes need to analyse based on FTIR results. The primary form of aluminium in GGBS is dominated by tetra-coordinated aluminium along with a few penta-coordination and hexa-coordination aluminium,,while more penta-coordination and hexa-coordination aluminium exist in MK, which is the main factor affecting the pozzolanic activation between different MK particles (Fig. 3). The structure of MK is decomposed to form a non-crystalline polymer of framework composed of Si-O and Al-O in the alkaline environment, prompting the transformation of aluminium with penta-coordination and hexa-coordination to tetra-coordination. Due to the complexity with co-existence, only the signals at around 1.9 ppm, 27 ppm, 59 ppm are considered symbols for determining and quantifying the tetra-coordinated, penta-coordinated and hexa-coordinated aluminium in unhydrated GGBS and MK, respectively, in the ^{27}Al NMR spectra, where the position of the peak in different specimens is slightly different due to the discrepancy of raw material properties and mix proportions (Love et al., 2007; Padilla-Encinas et al., 2020; Rocha, 2013; Sun et al., 2019). Regarding AH_3 gel, the position shifts from 11.5 ppm to 7.5 ppm with the change of crystallinity of the hydroxide, following a trend that a higher crystallinity generates higher ppm (Isobe et al., 2007; Padilla-Encinas et al., 2020; Skibsted et al., 1993; Zhang et al., 2018). In this study, the signal of AH_3 gel is determined at around 9 ppm. Based on the available information, the main peaks are deconvolved into a few peaks to identify the content of each hydration phase in all

mixtures.

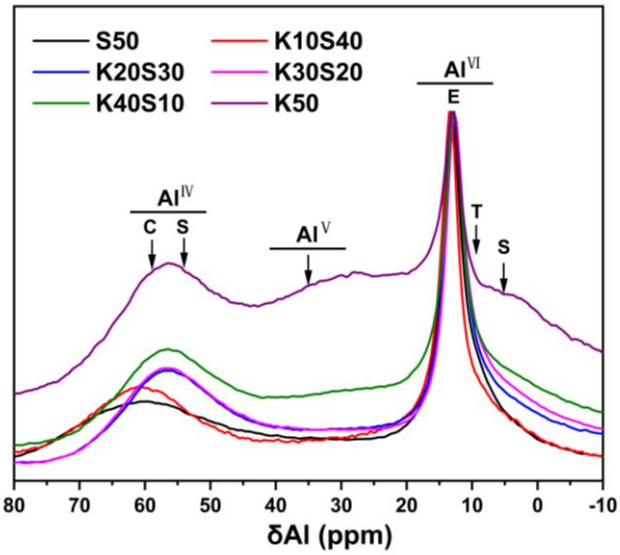

Fig. 12. ^{27}Al NMR spectra of ESPCM binders at 28 d. (This picture is optimised without change any data)

Fig. 13 demonstrates the deconvolution results, where the six signals are used to fit the occupied area in specimens, including hydration products and unhydrated GGBS and MK. Compared to the signal of ettringite with great crystallinity and a more orderly local environment (i.e., at 13 ppm), the signal of AH_3 gel (i.e., at 9 ppm) indicates a broader width. The incorporation of MK declines the area of ettringite but amplifies the area of AH_3 gel, implying that the absence of portlandite resists the generation of ettringite. The spectrum for K50 exhibits a stronger dispersity and ettringite signal is less intense due to a large accumulation of unhydrated MK. In addition, the enhancement of signals at 1.9 ppm, 27 ppm and 59 ppm can also be identified.

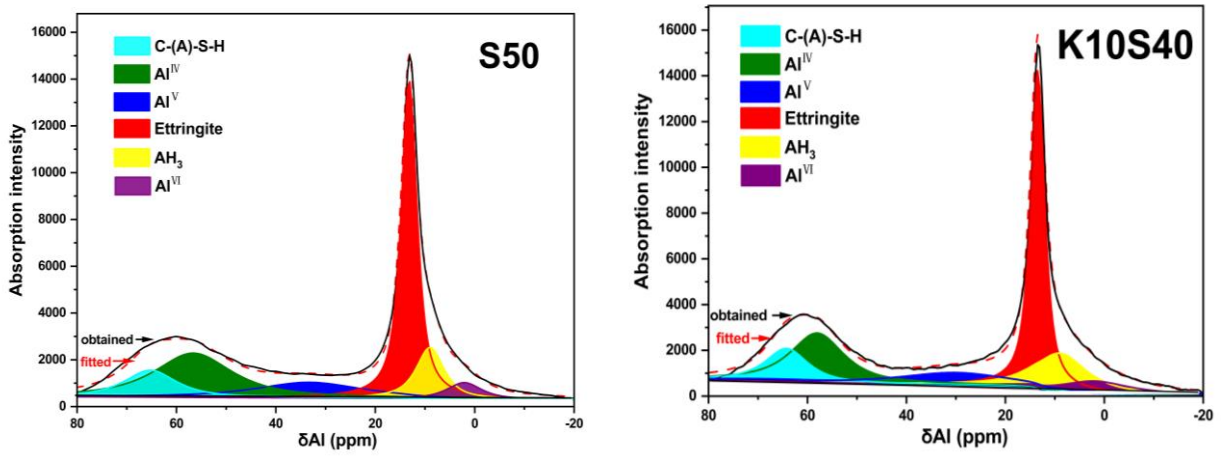

(a) (b)

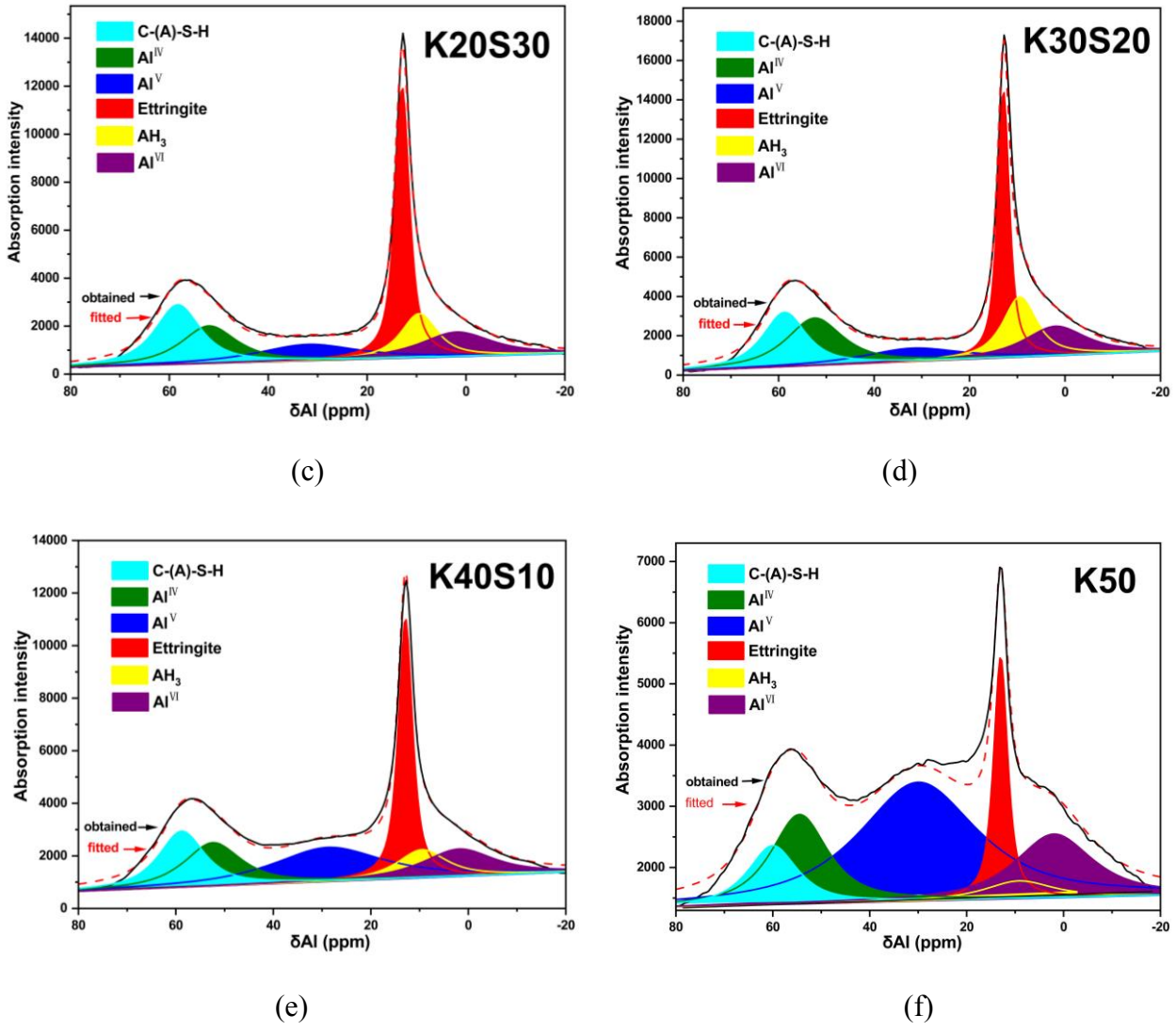

Fig. 13. ^{27}Al NMR deconvolution: A-S50; B-K10S40; C-K20S30; D-K30S20; E-K40S10; F-K50.

Fig. 14 shows the calculated relative proportion of phases containing aluminium, aiming to explore the underlying mechanisms. With the increase of MK content from 0% to 30%, the relative ratio of aluminium in C-A-S-H gel is increased from 7.47% to 17.71% and reaches 19.87% for specimen K20S30. In contrast, the relative ratio of aluminium in ettringite is inversely proportional to MK dosage and decreased from 35.87% (S50) to 9.67% (K50). As the reduction of GGBS dosage, which is regarded as the main producer of C-S-H gel in ESPCM pastes, the aluminium phase derived from MK tends to transfer into C-S-H gel rather than participants in the chemical reaction for the formation of ettringite. It is consistent with the finding in terms of the relationship between the GGBS content and cumulative heat release associated with C-S-H gel shown in Figs. 6 and 7. In general, the proportion of aluminium in ettringite is the highest, and more than 50% aluminium enters the hydration product in the pastes with no more than 30% MK. Moreover, the relative content of

aluminium with tetra-coordination decreases when the slag is substituted gradually, which is contrary to the penta-coordinated and hexa-coordinated aluminium.

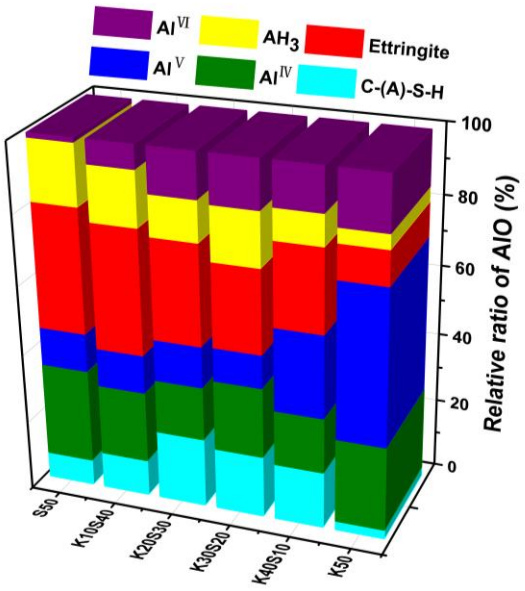

Fig. 14. Relative areas associated with AlO signals in ^{27}Al NMR spectra. (This picture is optimised without change any data)

The absolute quantification of the aluminium phase in all ESPCM pastes is calculated further according to the relative proportion and X-ray fluorescence spectrometer (XRF) analysis (Fig.15). With the further increase of MK, the quantity of aluminium incorporated C-S-H gel tends to increase and then declines and reaches 2.60% for K20S30 and 2.73% for K30S20, consistent with the FTIR analysis. The aluminium content in AH_3 gel exhibits the same tendency as it in C-(A)-S-H gel, while it presents the highest dosage (around 4.82%) for K40S10. Although the relative ratio of aluminium in ettringite decreases, the absolute content is still higher than that in specimen S50 (i.e., 3.01%) as the MK dosage is within 30%, where the changing trend is consistent with that of XRD analysis.

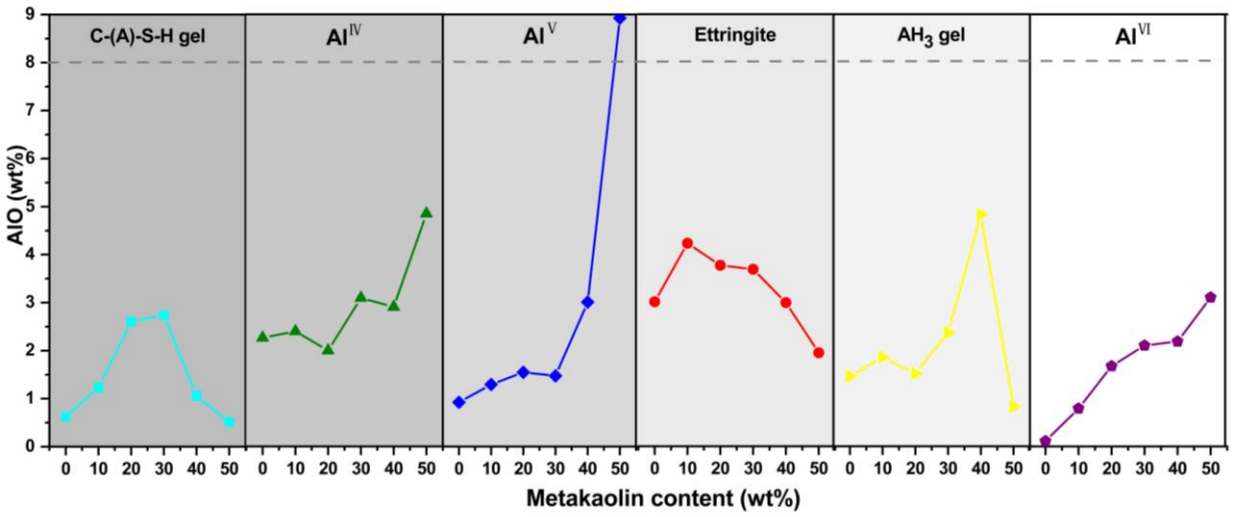

Fig. 15. Quantification of aluminium phase in ESPCM binders at 28 d.

Fig. 16 displays the DTG-DSC curves of all pastes. During the hydration reaction, free water inside ESPCM pastes is consumed and transformed to chemically bonded water in hydration products, including ettringite, C-(A)-S-H gel, and AH_3 gel, suggesting that the amount of hydration product in different temperature ranges can be roughly evaluated to verify the veracity of ^{27}Al NMR results. Similar to the curve of SSC (H. Park et al., 2016), two endothermic peaks can be observed in the range of 50 °C to 200 °C. In addition to the endothermic peak at around 85 °C to 140 °C (A Gruskovnjak et al., 2008) that is related to the generation of ettringite and C-(A)-S-H gel, the appearance of connective endothermic peak ranging from 140 °C to 180 °C determines the existence of unhydrated gypsum (Gijbels, Nguyen, et al., 2019; Hua et al., 1999). The endothermic peak aluminium-hydroxide located at 180 °C to 300 °C, which also appears as the shoulder of the decomposition peak of gypsum, is inconspicuous due to its low content and crystallinity (Gijbels, Nguyen, et al., 2019). However, the existence of AH_3 gel can be identified by the cleavage of the second peaks at DSC curves, which is also observed in FTIR spectra. No significant peak appears in the vicinity of 450 °C, representing the deficiency of portlandite (Bakolas et al., 2006), which is also in good agreement with the XRD analysis. The crystallization degree and granularity of ettringite would affect the temperature of decomposition. It has been demonstrated that the ettringite with high crystallization would dehydrate coordinated waters gradually in several periods: the amount of water is decomposed at 160 °C, while the rest about 8 molecules remains stable until the temperature exceeds 280 °C. A drop in crystallinity would move the heat-absorption peak forwards and accelerate the dehydration rate (Liu et al., 2019), indicating that the crystallization of ettringite is poor in ESPCM

pastes.

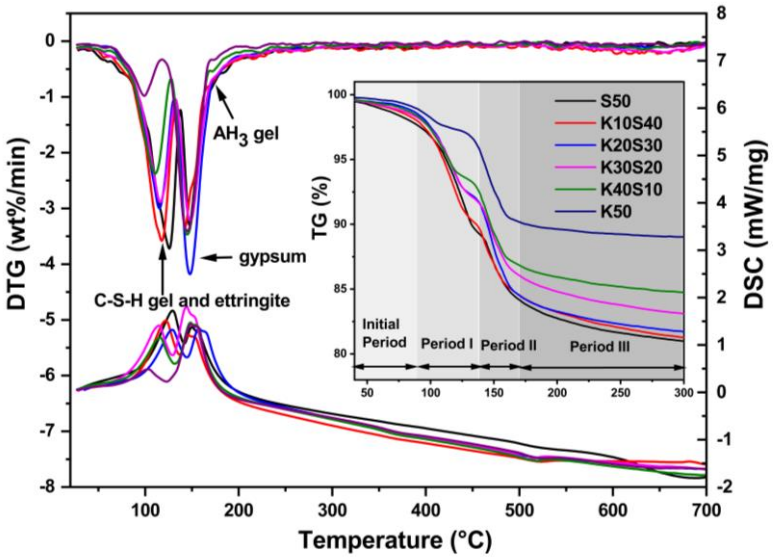

Fig. 16. DTG -DSC curves for ESPCM binders at 28 d.

The dehydration peak of gypsum is linked to that of hydration products, denoting that the two dehydration reactions occurred simultaneously, while it is difficult to quantify the total mass of each substance accurately. The quantity of hydration products can be evaluated with the mass loss, which is kept constant during the same periods. According to the rate of mass loss observed from the TG curve (Fig. 16), the region of 40-300 °C can be divided into four periods, as illustrated in Fig. 17, which shows a slight change in the range of temperature during the same period for pastes with different MK contents. The initial period assigned to the mass loss of physical water exhibits a declining trend (mass loss in the region of 2.74%-0.74%) with the increase of MK (0%-50%). A similar trend can be observed in period I that is attributed to the thermal decomposition of ettringite and C-(A)-S-H gel, where the mass loss is decreased from 8.67% (S50) to 1.55% (K50) when the GGBS is completely replaced. In proportion, the relative mass loss of unhydrated gypsum decreases with the increased hydration degree, leading to an opposite trend in period II. As the generation of AH_3 gel displays a slight effect on strength enhancement, no regular change can be observed in period III, where the mass loss maintains in the range of 0.88% (K50) to 2.36% (K30). This can be ascribed to the different chemical compositions and hydration behaviour that determine the different roles of MK and GGBS in ESPCMs. Compared to S50, the relative mass loss of hydration products (Fig. 17b) in periods I and III displays a decline with the addition of 10% MK and is even decreased more rapidly with the further incorporation of MK. This is due to the continuous generation of portlandite

as the hydration proceeds, which is only provided by the self-hydration of GGBS in the later period.

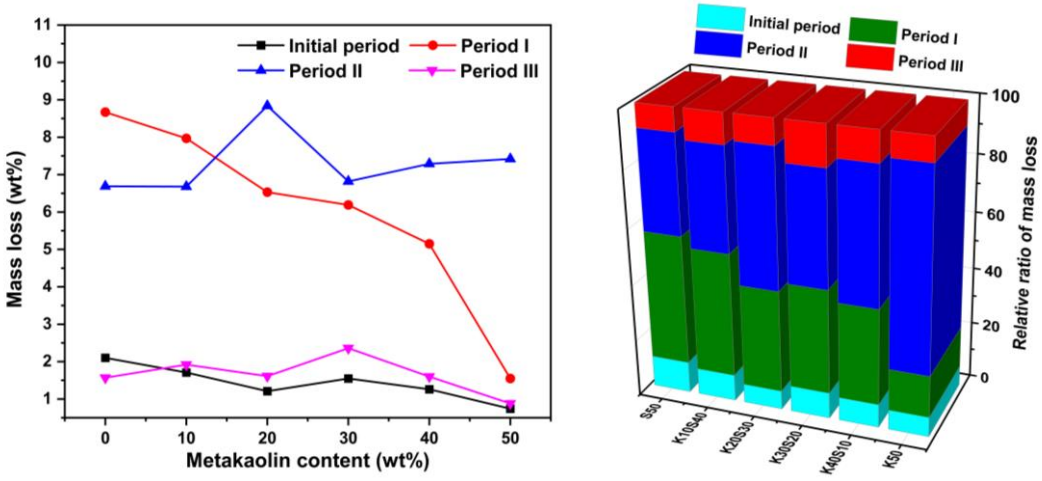

(a) (b)

Fig. 17. Characteristics of (a) mass loss and (b) relative ratio on the TG curves. (This picture is optimised without change any data)

The hydration process of the ESPCM can be summarised below. During the initial period, the hydration of cement produces portlandite to activate a part of GGBS and MK. As shown in Eqs. (3)-(4), the structure of GGBS with calcium aluminosilicate glass phase is depolymerized gradually, and the surface network structure such as Si-O···Ca···O-Si and Si-O···Ca···O-Al linked with Ca^{2+} or Mg^{2+} is destructed firstly with the action of OH^-, where the network-modifying bonds (e.g. Ca-O and Mg-O) is more easily destructed than the network-forming bonds (e.g. Si-O-Si and Si-O-Al) (Fernández-Jiménez et al., 2008; Gsa et al.; Mozgawa et al., 2009).

$$\equiv Si\text{-}O\cdots Ca\cdots O\text{-}Si \equiv + 2OH^- \rightarrow 2[\equiv Si\text{-}O\text{-}]^- + Ca(OH)_2 \quad (3)$$

$$\equiv Si\text{-}O\cdots Ca\cdots O\text{-}Al^- \equiv + 2OH^- \rightarrow 2[\equiv Si\text{-}O\text{-}]^- + [\equiv Al\text{-}O\text{-}]^- + Ca(OH)_2 \quad (4)$$

Following the dissolution of GGBS with an amorphous structure, portlandite forms continuously in the system and promotes further hydration of GGBS and MK, the internal Si-O-Si and Al-O link of which are destructed and the formed ion groups such as $Al(OH)_4^-$, $Al(OH)_5^{2-}$, $Al(OH)_6^{3-}$ (A. et al., 2003), $[SiO(OH)_3]^-$, $[SiO_2(OH)_2]^{2-}$ are released into pore solution, as expressed by: (Gsa et al.; Palou et al., 2017)

$$[\equiv Al\text{-}O\text{-}]^- + mOH^- \rightarrow Al(OH)_m^{3-m} \ (m=3, 4, 5, 6) \quad (5)$$

$$\equiv Si\text{-}O\text{-}Al^- + OH^- \rightarrow \equiv Si\text{-}OH + [\equiv Al\text{-}O\text{-}]^- \quad (6)$$

$$\equiv Si\text{-}O\text{-}Si \equiv + OH^- \rightarrow \equiv Si\text{-}OH + [\equiv Si\text{-}O\text{-}]^- \quad (7)$$

$$\equiv Si\text{-}OH + OH^- \rightarrow [SiO(OH)_3]^- \quad (8)$$

With the increase of silicon oxides and aluminium oxides monomers concentration, dimer structure (i.e., Si-O-Si and Al-O-Si) is reformed and polymerized in the existence of Ca^{2+}. As shown in Eqs. (9) and (10), C-(A)-S-H gel and ettringite are formed due to the reaction of $Al(OH)_4$ and $[SiO(OH)_3]$ with the presence of sulphate and portlandite (Deng et al., 2020; Mozgawa et al., 2009).

$$[\equiv Si\text{-}O\text{-}]^- + [\equiv Al\text{-}O\text{-}]^- + Ca^{2+} + OH^- \rightarrow C\text{-}(A)\text{-}S\text{-}H \quad (9)$$

$$2Al(OH)_4^- + 3CaSO_4 \cdot 2H_2O + 3Ca^{2+} + 4OH^- + 20H_2O \rightarrow 3CaO \cdot Al_2O_3 \cdot 3CaSO_4 \cdot 32H_2O \quad (10)$$

In the process of producing the hydrates, aluminium with three forms of coordination plays multiple structural roles. One migrates into the bridging silicon position of the silicon-oxygen tetrahedron in C-S-H gel and is formed as 4-coordination, which is beneficial for enhancing the structural stability of C-S-H gel and mechanical properties. In addition, it can also exist in C-S-H gel layers as penta-coordination. Although less C-S-H gel is formed with the further incorporation of MK, more aluminium is released to generate ettringite or migrate into C-S-H gel, while the excess part only enters the AH_3 gel due to the depletion of portlandite. Previous studies have pointed out that the aluminate and portlandite released by slag will form IP C-A-S-H gel with a dense structure to envelop the slag particle, inhibiting further hydration and ions release. Therefore, the content of aluminium in IP C-A-S-H gel is larger than OP C-A-S-H gel, where the AFm generated on origin distribution is also noticed. During the process of alkali-activated metakaolin, the aluminate with a higher dissolved rate than silicate is released into the pore solution for hydration due to the high dosage of Al□ with low chemical stability in metakaolin. More aluminium transfers into the C-S-H gel, leading to the generation of IP C-A-S-H gel with a relatively loose structure (B. Li, 2016; I. Richardson, 2004). Due to the larger solubility and interlayer size of C-A-S-H gel, the OH^- and silicate can shift and hydrate further, presenting the persistent enhancement on strength, which is also verified by the strength development test. (The previous studies are quoted to optimised the explanation)

However, the absence of portlandite has been demonstrated by the XRD and DTG-DSC analyses shown in Figs. 10 and 16, and it is impossible to activate all pozzolanic materials with such low content of cement. The glass phase dissolution of GGBS can produce portlandite to achieve self-hydraulics while MK cannot, indicating that GGBS as the sole calcium source for portlandite production affects the hydration process in the later period of hydration.

3.4 Pore structure characteristics

Table 5 presents the main pore structure characteristics, including porosity, critical pore size, and average pore size obtained from MIP. The specimen with no MK has the lowest porosity, i.e., 13.87%, and the porosity of pastes increases with the further incorporation of MK. The characteristic parameters of pore structure such as total volume, spatial distribution, medium pore size, and pore shape have a great influence on compressive strength (Aligizaki, 2006) and the pore size distribution changes depend on the hydration degree and grain size of the clinkers used. In this study, it can be found that the average pore size and critical pore size are decreased from 13.77 nm and 15 nm (S50) to 9 nm and 8 nm (K10S40), indicating that the specimen containing 10% MK may possess better mechanical properties and durability. It is also demonstrated that incorporating MK within 10% leads to a profound reduction in the micrometre-sized pores (around 50 nm) and critical pore size, as shown in Fig. 18. In addition, the porosity and other pore structure characteristics of pastes with 20% MK are higher than that of S50, as well as the volume of micrometre-sized pores. The pore size distribution shifts right with the increase of MK dosage, even the pore size for specimen K50 is concentrated at around 231 nm, implying a low degree of hydration. The formation of the coarse capillary pore (large than 100 nm) due to the addition of MK results in a looser pore structure, which contributes to the existence of gypsum crystal and the deficiency of C-(A)-S-H gel. Although no good correction between the porosity and the strength generally can be observed, improving pore structure presents a more significant enhancement on mechanical properties and durability.

Table 5. Pore structure characteristics of binders at 28 d.

Sample label	Porosity (%)	Critical pore size (nm)	Average pore size (nm)
S50	13.87	13.77	15
K10S40	22.67	9	8
K20S30	25.53	40	20
K30S20	35.27	226	23
K40S10	54.69	121	29
K50	37.52	230	401

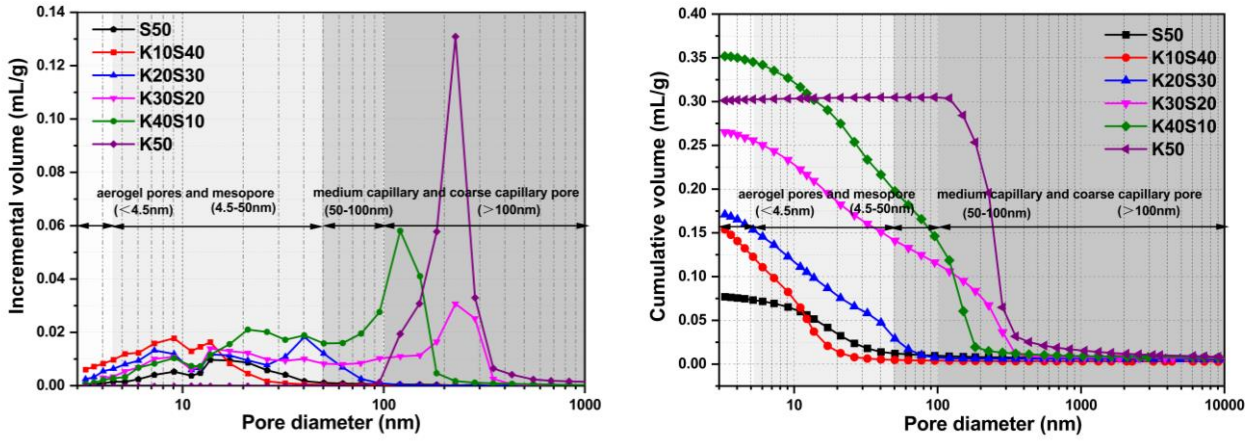

(a) (b)

Fig. 18. Pore size distribution curves of ESPCM binders at 28d (a) incremental intrusion and (b) cumulative intrusion (Adding Fig. 18b)

As seen in Fig. 19, the pore size distribution can be divided into four distinct ranges. The pore volume fraction of each part in each specimen is cumulated to estimate the effect of MK on the pore structure of ESPCM pastes. Regarding total porosity, the volume fraction of aerogel pores (less than 4.5 nm) occupies more than the mesopores (in the range of 4.5-50 nm), reaching 12.48% for the specimen containing 10% MK. Furthermore, the substitution of MK (0%-20%) leads to an increase in the volume fraction of mesopores from 73.91% to 77.81%, even the volume fraction of harmless pore (less than 50 nm) in the specimens K10S40 and K20S30 exceeds 80%, resulting in a refinement of pore size. Given that the enhancement in strength of paste can be generally induced by smaller-sized pores (Mehta et al., 2013), the compressive strength disparity is not only determined by the physical factors, e.g., filling effect or the morphological difference of the crystals, but also depends on the chemical factors including the quantity and type of hydration products (H. Park et al., 2016). However, the volume fraction of harmful pores (greater than 100 nm) increases significantly with the further addition of MK, exceeding 30%, due to the low hydration degree, which agrees well with the compressive strength test results (Fig. 20).

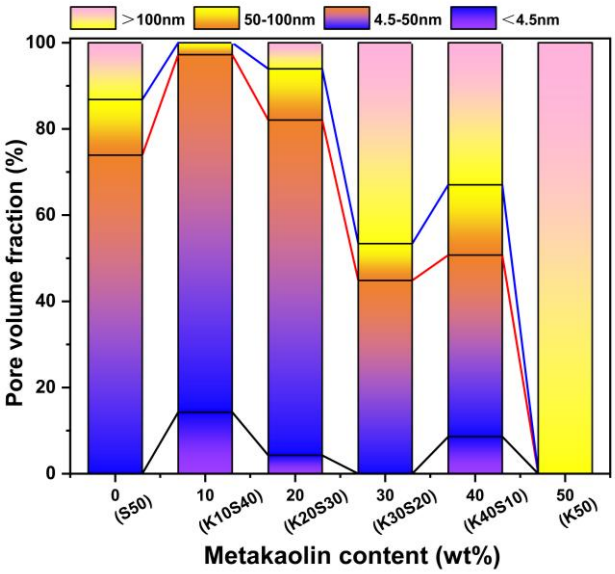

Fig. 19. Pore volume division of ESPCM binders at 28 d. (This picture is optimised without change any data)

3.5 Strength development

Fig. 20 shows the flexural and compressive strengths of ESPCM pastes at 3, 7, and 28 d, which drop with the increase of MK content from 10% to 50%. The specimens containing 10-20% GGBS can achieve a higher strength development at each curing age than S50. As seen in Fig. 20a, the maximum flexural strength at 3 d can be observed for specimens containing 10% and 20% MK, which is 12.5% higher than that of S50. A higher replacement level of GGBS (over 30%) causes a reduced strength at each curing age. A significant strength development can be observed for S50 at 7 d, which is 142.9% higher compared to that at 3 d. The pastes containing MK exhibit an noticeable strength enhancement at 28 d, where the 28-d flexural strength of pastes with 10% and 20% MK is increased by 18.9% and 16.5%, respectively, compared to S50, indicating the significant influence of MK on the strength of ESPCM pastes at 28 d.

A similar trend can be found for the compressive strength development, as demonstrated in Fig. 20b. The reference specimen without MK (S50) shows a rapid strength development during early ages, where more than 70% of its 28-d strength is developed within 7 d of curing. Though the rapid growth of early strength, S50 has a lower compressive strength than the specimen with 10% MK at each curing age. In contrast, the specimens containing MK exhibit a slower strength growth rate at early ages but has a profound enhancement at later ages. The drop of compressive strength of ESPCM paste is in proportion to the dosage of MK. When the GGBS is entirely replaced by MK, the strength

of the specimen develops slowly from 3 d to 28 d and only reaches 5 MPa. The effect of MK on compressive strength development varies with hydration time and dosage. After contact with water and up to 3 d of hydration, MK dosage shows a significant effect on the curing of pastes but negatively influences the compressive strength. As observed from the cumulative heat release curve, the strength is associated with the hydration degree characterised by heat release, and the slopes of the curve in different periods reflect the rate of hydration. The largest heat release can be found for K10S40, which agrees well with the results of compressive strength. When the replacement of GGBS by MK exceeds 30%, the slope of the cumulative heat release curve becomes flat after 10 h, suggesting a lower hydration rate and strength development in the later period. Compared to S50, the addition of MK at a dosage of 10% and 20% effectively enhances the compressive strength at 28 d, which achieves 60 MPa.

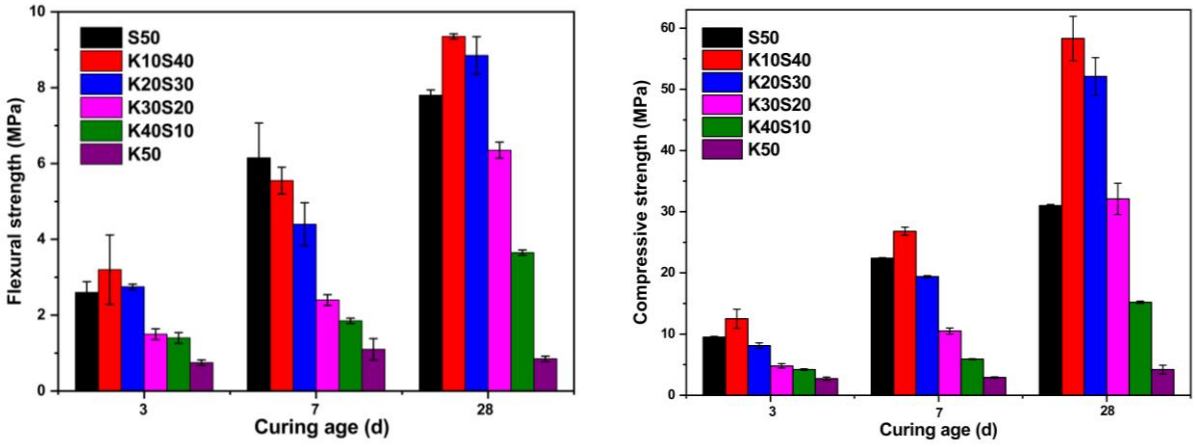

(a) (b)

Fig. 20. (a) Flexural and (b) compressive strength development of ESPCM pastes.

Fig. 21 shows the influence of ettringite generated on the strength development of ESPCM pastes based on the analysis of ^{27}Al NMR. There exhibits a linear relationship between flexural/compressive strength and ettringite content, indicating that the formation of ettringite contributes to the strength development. It is worth noting that a negligible discrepancy in ettringite content can be observed for specimens with 20%-30% MK, where the absolute content of aluminium phase in ettringite for K20S30 and K30S20 reaches 3.78% and 3.69%, respectively. However, the difference in compressive strength reaches 20MPa, suggesting that the generated ettringite is not the only factor to determine the strength development, which is also affected by other factors such as the content, type, and distribution of hydration products. The significant chemistry of Portland cement, characterised by the

higher content of calcium, would facilitate the generation of a large amount of C-S-H gel by hydration, while the addition of supplementary cementitious materials changes the composition and structure of generated hydration products, affecting the property development (Lothenbach et al., 2011). The low GGBS dosage has little effect on the volume fraction of generated portlandite compared with Portland cement. A blend of Portland cement with MK would decrease the portlandite content and increase the quantity of C-S-H gel with a lower Ca/Si, even promote the uptake of aluminium in C-S-H gel (I. Richardson et al., 1993) due to the low content of calcium in MK, as demonstrated by ^{27}Al NMR in Fig. 15. Although the adding an appropriate dosage of MK with higher activated aluminium can improve the generation of ettringite to fill the pores effectively and make the matrix denser, the excessive MK content would not be activated sufficiently due to the shortage of portlandite. The gypsum particles in the system cannot be wrapped and cemented together effectively to form a network due to the reduction in the generated C-(A)-S-H gel, which is mainly formed by the hydration of GGBS. Therefore, a blend of GGBS and MK may bring a synergistic effect, i.e., the continuous hydration of GGBS not only generates C-(A)-S-H gel and provides portlandite to react with MK in the later period. An appropriate ratio of GGBS and MK is required to ensure a sufficient existence of C-(A)-S-H gel to active the unhydrated particles and accelerate the formation of controllable ettringite, which not only improves the early strength development but also optimises the pore structure (Fig. 19) of ESPCM pastes.

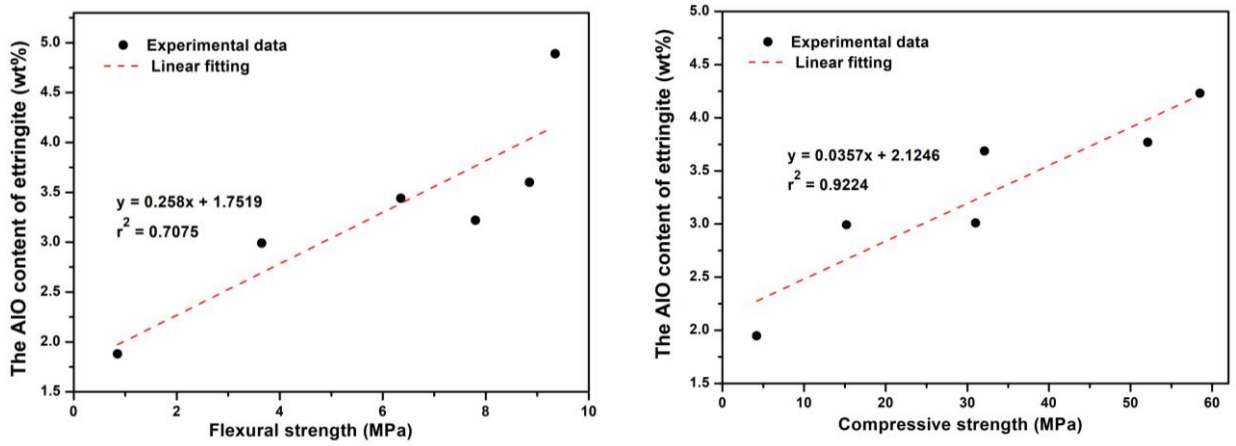

(a) (b)

Fig. 21. Ettringite content in relation to (a) flexural and (b) compressive strength of pastes.

4. Conclusions

In this study, towards the goal of expanding the application of ESPCMs, the effect of MK on early-

age hydration and microstructure evolution of ESPCM pastes with various GGBS dosages (0%-50%), as well as engineering properties including setting time, flexural and compressive strength, is investigated. Based on the experimental results, the conclusions can be drawn as follows:

- The incorporation of MK shortens the induction period of ESPCM pastes. A new peak in heat flow is identified, corresponding to a fast hydration period and a shortened setting time. The cumulative heat release of the main hydration peak in period III has a good relation to the GGBS content, suggesting that the excessive addition of MK may slow down generation of C-(A)-S-H gel and strength development.
- The change in the content of hydration products, including C-(A)-S-H gel, ettringite, and AH_3 gel, would directly affect the development of mechanical properties. As the MK dosage increases from 0% to 30%, more active aluminium phase is converted into C-S-H gel, which has a higher degree of polymerization and cross-linking, promoting the formation of ettringite. However, the content of C-(A)-S-H gel is inversely proportional to MK dosage.
- The porosity of ESPCM pastes is significantly increased by the reduction of GGBS. Compared to the sample including 50% GGBS, the pore size distribution of specimens containing no more than 20% MK shifts towards small pore size, including higher content of harmless pores (smaller than 50 nm), where the specimen containing 10% MK exhibits the highest volume fraction of aerogel pores (12.48%) and smallest average pore size (8 nm) and critical pore size (9 nm). When the substitution of GGBS by MK exceeds 30%, the high proportion of harmful pores (larger than 100 nm) leads to a loose pore structure.
- As the MK content increases from 0% to 50%, the setting time of ESPCM pastes is decreased by around 50%, while the flexural and compressive strengths are firstly increased and then decreased as the generation of portlandite directly affects the rate and degree of hydration. The compressive strength of ESPCM paste is enhanced by 70% and reaches 60 MPa when 10%-20% GGBS is substituted by MK, while the flexural strength tends to be stable and maintains around 9 MPa. In addition, there exists a linear relationship between the strength development and the content of aluminium phase in ettringite, indicating that the generation of ettringite can help improve the microstructure and result in acceptable mechanical properties of ESPCM paste.
- Differences in chemical composition between GGBS and MK lead to varied effects on hydration of ESPCMs. GGBS with high calcium can produce portlandite for the generation of C-(A)-S-H

gel and ettringite, while MK cannot. A synergistic effect of blended GGBS and MK indicates that the optimal MK dosage should be limited to 20%.

- As the primary hydration products of ESPCM, ettringite is carbonated easily especially in the absence of portlandite (Seo et al., 2021), which makes this cementitious material vulnerable to carbonation, limiting its actual application. Little research has studied the effect mechanism of carbonation on the microstructure and properties of ESPCM pastes, and suitable methods need to be developed to improve the carbonization resistance.

Acknowledgements

The authors gratefully acknowledge the financial support from the Key Research and Development Program of Hubei Province (2020BAB065), the Third Batch of Special Fund for Science and Technology Development of Zhongshan City in 2020 (2020-18), the Sanya Yazhou Bay Science and Technology City Administration (No. SKJC-KJ-2019KY02), Fundamental Research Funds for the Central Universities (Nos. 2020III042 and 205259003), major science and technology project in Zhongshan city (No. 200825093739256), Hubei Key Laboratory of Roadway Bridge and Structure Engineering (No. DQJJ201902), and China Scholarship Council. The financial support provided by the Engineering and Physical Sciences Research Council (EPSRC), UK under Grant No. EP/R041504/1 and the Royal Society, UK under Award No. IEC\NSFC\191417 as well as the Visiting Researcher Fund Program of State Key Laboratory of Water Resources and Hydropower Engineering Science, China under Award No. 2019SGG01 to M. Zhang is greatly acknowledged.

References

A., Palomo, and, J., I., López, dela, & Fuente. (2003). Alkali-activated cementitous materials: Alternative matrices for the immobilisation of hazardous wastes: Part I. Stabilisation of boron. *Cement and Concrete Research*, 281-288.

Aligizaki, K. K. (2006). *Pore Structure of Cement-Based Materials: Testing, Interpretation and Requirements*: Pore Structure of Cement-Based Materials: Testing, Interpretation and Requirements.

Andersen, M., Jakobsen, H. J., & Skibsted, J. (2003). Incorporation of aluminum in the calcium silicate hydrate (C-S-H) of hydrated portland cements: a high-field ^{27}Al and ^{29}Si MAS NMR investigation. *Inorganic Chemistry, 42*(7), 2280-2287.

Andrade, D. S., Rêgo, J. S., Morais, P., Neiry, D., & Rojas, M. F. (2019). Investigation of C-S-H in ternary cement pastes containing nanosilica and highly-reactive supplementary cementitious materials (SCMs): Microstructure and strength. *Construction and Building Materials, 198*, 445-455.

Bakolas, A., Aggelakopoulou, E., Moropoulou, A., & Anagnostopoulou, S. (2006). Evaluation of pozzolanic activity and physicomechanical characteristics in metakaolin-lime pastes. *Journal of Thermal Analysis and Calorimetry, 84*(1), 157-163.

Barnes, P., & Bensted, J. (2002). *Structure and performance of cements*: CRC Press.

Bernal, S. A., Provis, J. L., Rose, V., & Gutierrez, R. (2011). Evolution of binder structure in sodium silicate-activated slag-metakaolin blends. *Cement and Concrete Composites, 33*(1), 46-54.

Bijen, J., & Niël, E. (1981). Supersulphated cement from blastfurnace slag and chemical gypsum available in the Netherlands and neighbouring countries. *Cement and Concrete Research, 11*(3), 307-322.

Bishop, M., Bott, S. G., & Barron, A. R. (2003). A new mechanism for cement hydration inhibition: solid-state chemistry of calcium nitrilotris (methylene) triphosphonate. *Chemistry of materials, 15*(16), 3074-3088.

Boháč, M., Palou, M., Novotný, R., Másilko, J., Všianský, D., & Staněk, T. (2014). Investigation on early hydration of ternary Portland cement-blast-furnace slag–metakaolin blends. *Construction and Building Materials, 64*, 333-341.

Bosque, I. S. D., Martínez-Ramírez, S., & Blanco-Varela, M. T. (2014). FTIR study of the effect of temperature and nanosilica on the nano structure of C-S-H gel formed by hydrating tricalcium silicate. *Construction and Building Materials, 52*, 314-323.

Caladrone, M., Gruber, K., & Burg, R. (1994). High reactivity metakaolin: A. New generation of mineral admixture. *Concrete International. Now, 16*(11), 32-40.

Chao, L., Sun, H., & Li, L. (2010). A review: The comparison between alkali-activated slag (Si+Ca) and metakaolin (Si+Al) cements. *Cement and Concrete Research, 40*(9), 1341-1349.

Collepardi, M., Baldini, G., M. Pauri, & Corradi, M. (1978). Tricalcium aluminate hydration in the presence of lime, gypsum or sodium sulfate. *Cement and Concrete Research, 8*(5), 571-580.

COLLEPARDI, M., BALDINI, G., PAURI, M., & CORRADI, M. (1979). Retardation of tricalcium aluminate hydration by calcium sulfate. *Journal of the American Ceramic Society, 62*(1-2), 33-35.

Deng, G., He, Y., Lu, L., & Hu, S. (2020). The effect of activators on the dissolution characteristics and occurrence state of aluminum of alkali-activated metakaolin. *Construction and Building Materials, 235*(12), 117451.

do Carmo Holanda, F., Schmidt, H., & Quarcioni, V. A. (2017). Influence of phosphorus from phosphogypsum on the initial hydration of Portland cement in the presence of superplasticizers. *Cement and concrete composites, 83*, 384-393.

Duchesne, J., & Be, M. (1995). Effect of supplementary cementing materials on the composition of cement hydration products. *Advanced Cement Based Materials, 2*(2), 43-52.

Fang, G., & Zhang, M. (2020). Multiscale micromechanical analysis of alkali-activated fly ash-slag paste. *Cement and Concrete Research, 135*, 106141.

Fernández-Jiménez, A., Monzó, M., Vicent, M., Barba, A., & Palomo, A. (2008). Alkaline activation of metakaolin–fly ash mixtures: Obtain of Zeoceramics and Zeocements. *Microporous and Mesoporous Materials, 108*(1–3), 41-49.

Fernández-Jiménez, A., & Palomo, A. (2005). Mid-infrared spectroscopic studies of alkali-activated fly ash structure. *Microporous & Mesoporous Materials, 86*(1-3), 207-214.

Fraire-Luna, P., Escalante-Garcia, J., & Gorokhovsky, A. (2006). Composite systems fluorgypsum–blastfurnance slag–metakaolin, strength and microstructures. *Cement and Concrete Research, 36*(6), 1048-1055.

Gijbels, K., Iacobescu, R. I., Pontikes, Y., Schreurs, S., & Schroeyers, W. (2019). Alkali-activated binders based on ground granulated blast furnace slag and phosphogypsum. *Construction and Building Materials, 215*, 371-380.

Gijbels, K., Nguyen, H., Kinnunen, P., Schroeyers, W., Pontikes, Y., Schreurs, S., & Illikainen, M. (2019). Feasibility of incorporating phosphogypsum in ettringite-based binder from ladle slag. *Journal of Cleaner Production, 237*, 117793.

Glukhovsky, V., Rostovskaja, G., & Rumyna, G. (1980). *High strength slag-alkaline cements.* Paper presented at the Proceedings of the seventh international congress on the chemistry of cement.

Gruskovnjak, A., Lothenbach, B., Winnefeld, F., Figi, R., Ko, S.-C., Adler, M., & Mäder, U. (2008). Hydration mechanisms of super sulphated slag cement. *Cement and Concrete Research, 38*(7), 983-992.

Gruskovnjak, A., Lothenbach, B., Winnefeld, F., Münch, B., Figi, R., Ko, S.-C., . . . Mäder, U. (2011). Quantification of hydration phases in supersulfated cements: review and new approaches. *Advances in cement research, 23*(6), 265-275.

Gsa, B., Jz, B., & Na, Y. B. Microstructural evolution and characterization of ground granulated blast furnace slag in variant pH - ScienceDirect. *Construction and Building Materials, 251*.

Hargis, C. W., A.P. Kirchheim, Monteiro, P. J., & Gartner, E. M. (2013). Early age hydration of calcium sulfoaluminate (synthetic ye'elimite, C_4A_3S) in the presence of gypsum and varying amounts of calcium hydroxide. *Cement and Concrete Research, 48*, 105-115.

Hewlett, P., & Liska, M. (2019). *Lea's chemistry of cement and concrete*: Butterworth-Heinemann

Hua, C., Pei, J. H., & Hou, S. C. (1999). Application of thermo-Raman spectroscopy to study dehydration of $CaSO_4 \cdot 2H_2O$ and $CaSO_4 \cdot 0.5H_2O$. *Materials Chemistry and Physics, 58*(1), 12-19.

Huang, Y., & Lin, Z. (2010). Investigation on phosphogypsum–steel slag–granulated blast-furnace slag–limestone cement. *Construction and Building Materials, 24*(7), 1296-1301.

Ioannou, A., & Dimirkou, A. (1997). Phosphate adsorption on hematite, kaolinite, and kaolinite–hematite (k–h) systems as described by a constant capacitance model. *Journal of colloid and interface science, 192*(1), 119-128.

Isobe, T., Watanabe, T., Caillerie, J., Legrand, A. P., & Massiot, D. (2007). Solid-state ^{1}H and ^{27}Al NMR studies of amorphous aluminum hydroxides. *Journal of colloid and interface science, 261*(2), 320-324.

Jha, V. K., Kameshima, Y., Nakajima, A., & Okada, K. (2008). Utilization of steel-making slag for the uptake of ammonium and phosphate ions from aqueous solution. *Journal of hazardous materials, 156*(1-3), 156-162.

Jiahui, P., Zhihui, P., Jianxin, Z., & Tizhi, W. Study on the form and distribution of water-solution P_2O_5 in phosphor gypsum and effective mechanism of properties. *Journal of the Chinese Ceramic Society, 28(4) (2000) 309–313.*

Jin, X., & Li, Z. (2003). Effects of mineral admixture on properties of young concrete. *Journal of materials in civil engineering, 15*(5), 435-442.

Kapeluszna, E., Kotwica, L., Rozycka, A., & Golek, L. (2017). Incorporation of Al in C-A-S-H gels with various Ca/Si and Al/Si ratio: Microstructural and structural characteristics with DTA/TG, XRD, FTIR and TEM analysis. *Construction and Building Materials, 155*(nov.30), 643-653.

L.Frost, R., Lópeza, A., Yunfei, X., Scholzb, R., Costac, G. M., Limad, R. M. F., & Granjab, A. (2013). The spectroscopic characterization of the sulphate mineral ettringite from Kuruman manganese deposits, South Africa. *Vibrational Spectroscopy, 48*, 266-271.

Landry, C. J., Koretsky, C. M., Lund, T. J., Schaller, M., & Das, S. (2009). Surface complexation modeling of Co (II) adsorption on mixtures of hydrous ferric oxide, quartz and kaolinite. *Geochimica et Cosmochimica Acta, 73*(13), 3723-3737.

Li, B. (2016). *Research on microstructure characterization and cementious ability of C-A-S-H gel*

modified with Polyaluminum chloride. (Graduat), Wuhan university of Technology, Wuhan.

Li, X., Du, J., Gao, L., He, S., Gan, L., Sun, C., & Shi, Y. (2017). Immobilization of phosphogypsum for cemented paste backfill and its environmental effect. *Journal of Cleaner Production, 156*, 137-146.

Lin, Z., & Huang, Y. (2009). Investigation on Phosphogypsum-base Non-calcined Cement. *Journal of Wuhan University of Technology, 31*(4), 53-55.

Lin, Z., Huang, Y., & Shui, Z. (2010). *Excess-Sulfate Phosphogypsum Slag Cement and Concrete*. Wuhan Wuhan University of Technology Press.

Liu, S., Wang, L., & Yu, B. (2019). Effect of modified phosphogypsum on the hydration properties of the phosphogypsum-based supersulfated cement. *Construction and Building Materials, 214*, 9-16.

Lothenbach, B., Scrivener, K., & Hooton, R. (2011). Supplementary cementitious materials. *Cement and Concrete Research, 41*(12), 1244-1256.

Love, C. A., Richardson, I. G., & Brough, A. R. (2007). Composition and structure of C–S–H in white Portland cement–20% metakaolin pastes hydrated at 25 °C. *Cement and Concrete Research, 37*(2), 109-117.

M.K.Z. L.N. Zhou, Q. L. Z. Effects of different modification methods on coagulant properties of phosphogypsum cement. *Cement and Concrete Composites, 8 (2007) 16-18.*

Magallanes-Rivera, R., & Escalante-García, J. (2014). Anhydrite/hemihydrate-blast furnace slag cementitious composites: Strength development and reactivity. *Construction and Building Materials, 65*, 20-28.

Matschei, T., Bellmann, F., & Stark, J. (2005). Hydration behaviour of sulphate-activated slag cements. *Advances in cement research, 17*(4), 167-178.

Mehta, P. K., & Monteiro, P. (2013). *Concrete : microstructure, properties, and materials*.

Michel, M., Georgin, J.-F., Ambroise, J., & Péra, J. (2011). The influence of gypsum ratio on the mechanical performance of slag cement accelerated by calcium sulfoaluminate cement. *Construction and Building Materials, 25*(3), 1298-1304.

Min, S. K., Jun, Y., Lee, C., & Oh, J. E. (2013). Use of CaO as an activator for producing a price-competitive non-cement structural binder using ground granulated blast furnace slag. *Cement and Concrete Research, 54*, 208-214.

Moore, A., & Taylor, H. (1970). Crystal structure of ettringite. *Acta Crystallographica Section B: Structural Crystallography and Crystal Chemistry, 26*(4), 386-393.

Mozgawa, W., & Deja, J. (2009). Spectroscopic studies of alkaline activated slag geopolymers. *Journal of Molecular Structure, 924*(none), 434-441.

Myers, R. J., Bernal, S. A., Gehman, J. D., van Deventer, J. S., & Provis, J. L. (2015). The Role of Al in cross-linking of alkali-activated slag cements. *Journal of the American Ceramic Society, 98*(3), 996-1004.

Myneni, S. C. B., Traina, S. J., Waychunas, G. A., & Logan, T. J. (1998). Vibrational spectroscopy of functional group chemistry and arsenate coordination in ettringite. *Geochimica et Cosmochimica Acta*.

Nabbou, N., Belhachemi, M., Boumelik, M., Merzougui, T., Lahcene, D., Harek, Y., . . . Jeguirim, M. (2019). Removal of fluoride from groundwater using natural clay (kaolinite): Optimization of adsorption conditions. *Comptes Rendus Chimie, 22*(2-3), 105-112.

Padilla-Encinas, P., Palomo, A., Blanco-Varela, M. T., & Fernández-Jiménez, A. (2020). Calcium sulfoaluminate clinker hydration at different alkali concentrations. *Cement and Concrete*

Research, 138, 106251.

Palou, M., Kuzielová, E., Žemlička, M., Novotný, R., & Másilko, J. (2017). The effect of metakaolin upon the formation of ettringite in metakaolin–lime–gypsum ternary systems. *Journal of Thermal Analysis and Calorimetry, 133*(1), 73-86.

Pardal, X., Brunet, F., Charpentier, T., Pochard, I., & Nonat, A. (2012). Al-27 and Si-29 Solid-State NMR Characterization of Calcium-Aluminosilicate-Hydrate. *Inorganic Chemistry, 51*(3), 1827-1836.

Park, H., Jeong, Y., Jun, Y., Jeong, J.-H., & Oh, J. E. (2016). Strength enhancement and pore-size refinement in clinker-free CaO-activated GGBFS systems through substitution with gypsum. *Cement and Concrete Composites, 68*, 57-65.

Park, S. M., Jang, J. G., Lee, N., & Lee, H.-K. (2016). Physicochemical properties of binder gel in alkali-activated fly ash/slag exposed to high temperatures. *Cement and Concrete Research, 89*, 72-79.

Peng, J. H., Peng, Z. H., Zhang, J. X., & Wan, T. Z. (2000). Study on the form and distribution of water-soluble P_2O_5 in phosphogypsum and effective mechanism of properties. *Journal of the Chinese Ceramic Society, 28*(4), 309-313.

Puligilla, S., & Mondal, P. (2015). Co-existence of aluminosilicate and calcium silicate gel characterized through selective dissolution and FTIR spectral subtraction. *Cement and Concrete Research, 70*, 39-49.

Qian, J., Jincheng, Y. U., Sun, H., & Ying, M. A. (2017). Formation and Function of Ettringite in Cement Hydrates. *Journal of the Chinese Ceramic Society*, 1569-1581.

Radwan, M., & Heikal, M. (2003). Hydration characteristics of tetracalcium aluminoferrite phase in mixes containing β-hemihydate and phosphogypsum. *Journal of materials science, 38*(22), 4499-4505.

Radwan, M., & Heikal, M. (2005). Hydration characteristics of tricalcium aluminate phase in mixes containing β-hemihydate and phosphogypsum. *Cement and Concrete Research, 35*(8), 1601-1608.

Richardson, I. (2004). Tobermorite/jennite-and tobermorite/calcium hydroxide-based models for the structure of C-S-H: applicability to hardened pastes of tricalcium silicate, β-dicalcium silicate, Portland cement, and blends of Portland cement with blast-furnace slag, metakaolin, or silica fume. *Cement and Concrete Research, 34*(9), 1733-1777.

Richardson, I., & Groves, G. (1993). The incorporation of minor and trace elements into calcium silicate hydrate (C-S-H) gel in hardened cement pastes. *Cement and Concrete Research, 23*(1), 131-138.

Richardson, I. G. (2000). The Nature of the Hydration Products in Hardened Cement Pastes. *Cement and Concrete Composites, 22*(2), 97-113.

Rocha, J. (2013). Single- and Triple-Quantum 27Al MAS NMR Study of the Thermal Transformation of Kaolinite. *J. Metal. Sci., 7*(44), 24-27.

Scholtzová, E., Kucková, L., Koíek, J., & Tunega, D. (2015). Structural and spectroscopic characterization of ettringite mineral –combined DFT and experimental study. *Journal of Molecular Structure, 1100*, 215-224.

Scrivener, K., Snellings, R., & Lothenbach, B. (2016). *A Practical Guide to Microstructural Analysis of Cementitious Materials*: CRC Press, .

Seo, J., Yoon, H., Kim, S., Wang, Z., Kil, T., & Lee, H.-K. (2021). Characterization of reactive MgO-modified calcium sulfoaluminate cements upon carbonation. *Cement and Concrete Research, 146*, 106484.

Shi, C., & Day, R. L. (1995). Acceleration of the reactivity of fly ash by chemical activation. *Cement and Concrete Research, 25*(1), 15-21.

Singh, M., & Garg, M. (2002). Calcium sulfate hemihydrate activated low heat sulfate resistant cement. *Construction and Building Materials, 16*(3), 181-186.

Skibsted, J., Henderson, E., & Jakobsen, H. J. (1993). Characterization of calcium aluminate phases in cements by 27Al MAS NMR spectroscopy. *Inorganic Chemistry, 32*(6), 1013-1027.

Song, S., & Jennings, H. M. (1999). Pore solution chemistry of alkali-activated ground granulated blast-furnace slag. *Cement and Concrete Research, 29*(2), 159-170.

Song, S., Sohn, D., Jennings, H., & Mason, T. O. (2000). Hydration of alkali-activated ground granulated blast furnace slag. *Journal of materials science, 35*(1), 249-257.

Souza, P. S. L., & Dal Molin, D. C. (2005). Viability of using calcined clays, from industrial by-products, as pozzolans of high reactivity. *Cement and Concrete Research, 35*(10), 1993-1998.

Speight, J. G. (2017). *Lange's handbook of chemistry*: McGraw-Hill Education.

Standard, C. N. (1999). GB/T1767-1999: Method of testing cements-Determination of strength. In. Beijing: N.C.S. Committee.

Strandard, C. N. (2011). GB/T 1346-2001: Test methods for water requirement of normal consistency, setting time and soundness of the Portland cements,. In. Beijing: N.C.S. Committee.

Sun, T. (2019). Study on the optimum technological parameters of preparation of metakaolin with high activity. *China Cement, 12(1671-8321)* 94-95.

Sun, T., Ge , K., Wang, G., Ge Ng, H., & Chen, M. (2019). Comparing pozzolanic activity from thermal-activated water-washed and coal-series kaolin in Portland cement mortar. *Construction and Building Materials, 227*, 117092-.

Tabikh, A., & Miller, F. (1971). The nature of phosphogypsum impurities and their influence on cement hydration. *Cement and Concrete Research, 1*(6), 663-678.

Tafraoui, A., Escadeillas, G., Lebaili, S., & Vidal, T. (2009). Metakaolin in the formulation of UHPC. *Construction and Building Materials, 23*(2), 669-674.

Taher, M. (2007). Influence of thermally treated phosphogypsum on the properties of Portland slag cement. *Resources, Conservation and Recycling, 52*(1), 28-38.

Taylor, H. (1993). Nanostructure of C-S-H: Current status. *Adv. Cem. Based. Mater., 1*(1), 38–46.

Wang, L., Li, m., & Wang, B. (2003). Research status and prospect of metakaolin. *Academic Papers on Architecture and Civil Engineering*, 16-19.

Wei, J., & Gencturk, B. (2019). Hydration of ternary Portland cement blends containing metakaolin and sodium bentonite. *Cement and Concrete Research, 123*, 105772.

Wei, S., Tan, W., Liu, F., Zhao, W., & Weng, L. (2014). Surface properties and phosphate adsorption of binary systems containing goethite and kaolinite. *Geoderma, 213*, 478-484.

Yuheng, B., He, L., Yi, G., & Weiguo, Z. (2006). Research on Structure and Absorption Performance of Modified Kaolin Material with Large Surface Area, . *Non-Metallic. Mines., 2*.

Zhang, Y., & Chang, J. (2018). Microstructural evolution of aluminum hydroxide gel during the hydration of calcium sulfoaluminate under different alkali concentrations. *Construction and Building Materials, 180*, 655-664.